Neural Texture Splatting: Expressive 3D Gaussian Splatting for View Synthesis, Geometry, and Dynamic Reconstruction

YIMING WANG, ETH Zurich, Switzerland SHAOFEI WANG, ETH Zurich, Switzerland MARKO MIHAJLOVIC, ETH Zurich, Switzerland SIYU TANG, ETH Zurich, Switzerland

By and the seconstruction (6 input videos) Geometry Reconstruction Geometry Reconstruction Geometry Reconstruction Geometry Reconstruction Government of the seconstruction (10 input views) Sparse-View Reconstruction (10 input views) Dense-View Reconstruction Graph (Supplied Supplied Supplied

Fig. 1. **Neural Texture Splatting (NTS)** augments 3D Gaussian Splatting (3DGS) with neural RGBA fields per primitive, offering a plug-and-play module that boosts performance across multiple applications. We show that NTS significantly enhances the quality of sparse-view reconstruction for static and dynamic scenes, while also achieving noticeable improvements on geometry reconstruction and novel view synthesis under dense training views.

3D Gaussian Splatting (3DGS) has emerged as a leading approach for highquality novel view synthesis, with numerous variants extending its applicability to a broad spectrum of 3D and 4D scene reconstruction tasks. Despite its success, the representational capacity of 3DGS remains limited by the use of 3D Gaussian kernels to model local variations. Recent works have proposed to augment 3DGS with additional per-primitive capacity, such as per-splat textures, to enhance its expressiveness. However, these persplat texture approaches primarily target dense novel view synthesis with a reduced number of Gaussian primitives, and their effectiveness tends to diminish when applied to more general reconstruction scenarios. In this paper, we aim to achieve concrete performance improvement over state-ofthe-art 3DGS variants across a wide range of reconstruction tasks, including novel view synthesis, geometry and dynamic reconstruction, under both sparse and dense input settings. To this end, we introduce Neural Texture Splatting (NTS). At the core of our approach is a global neural field (represented as a hybrid of a tri-plane and a neural decoder) that predicts local

Authors' Contact Information: Yiming Wang, wangyim@ethz.ch, ETH Zurich, Switzerland; Shaofei Wang, sfwang0928@gmail.com, ETH Zurich, Switzerland; Marko Mihajlovic, marko.mihajlovic@inf.ethz.ch, ETH Zurich, Switzerland; Siyu Tang, siyu.tang@inf.ethz.ch, ETH Zurich, Switzerland.



This work is licensed under a Creative Commons Attribution 4.0 International License. SA Conference Papers '25, Hong Kong, Hong Kong © 2025 Copyright held by the owner/author(s). ACM ISBN 979-8-4007-2137-3/2025/12 https://doi.org/10.1145/3757377.3763957

appearance and geometric fields for each primitive. By leveraging this shared global representation that models local texture fields across primitives, we significantly reduce model size and facilitate efficient global information exchange, demonstrating strong generalization across tasks. Furthermore, our neural modeling of local texture fields introduces expressive view- and time-dependent effects, a critical aspect that existing methods fail to account for. Extensive experiments show that Neural Texture Splatting consistently improves models and achieves state-of-the-art results across multiple benchmarks. Project website: https://19reborn.github.io/nts/.

${\tt CCS\ Concepts: \bullet\ Computing\ methodologies} \rightarrow {\tt Rendering;\ Point-based\ models}.$

Additional Key Words and Phrases: Novel View Synthesis, 3D Gaussian Splatting, Static Reconstruction, Sparse-view Reconstruction, Dynamic Reconstruction

ACM Reference Format:

Yiming Wang, Shaofei Wang, Marko Mihajlovic, and Siyu Tang. 2025. Neural Texture Splatting: Expressive 3D Gaussian Splatting for View Synthesis, Geometry, and Dynamic Reconstruction . In SIGGRAPH Asia 2025 Conference Papers (SA Conference Papers '25), December 15–18, 2025, Hong Kong, Hong Kong. ACM, New York, NY, USA, 16 pages. https://doi.org/10.1145/3757377. 3763957

1 Introduction

Neural radiance fields (NeRFs [Mildenhall et al. 2020]) have demonstrated remarkable success in reconstructing scenes from calibrated

RGB captures. They have been widely applied across various 3D reconstruction tasks, showing promise in applications such as AR/VR, robotics, gaming, and 3D content creation [Tewari et al. 2022]. Recently, 3D Gaussian Splatting (3DGS) [Kerbl et al. 2023] has emerged as an efficient alternative to NeRFs by representing radiance fields as collections of 3D Gaussian primitives. This explicit, point-based representation enables both high-quality and real-time rendering. It has also been extended to tasks such as surface reconstruction [Huang et al. 2024; Yu et al. 2024d], sparse-view reconstruction [Mihajlovic et al. 2024b], and dynamic scene modeling [Lei et al. 2024; Qian et al. 2024; Sun et al. 2024; Wu et al. 2024a; Zhu et al. 2024].

However, the representational capacity of each primitive in 3DGS is inherently limited by the simplistic assumption of Gaussian kernels, making it difficult to capture high-frequency details and complex variations in appearance and geometry. Recent works have sought to enhance this capacity by incorporating per-splat 2D texture mappings [Chao et al. 2024; Rong et al. 2024] or modifying the Gaussian kernel distribution [Li et al. 2025; Zhu et al. 2025], showing promising improvements in novel view synthesis through increased local expressiveness.

Despite these advances, such methods are typically designed for novel view synthesis using dense training views and a reduced number of Gaussian primitives, while forgoing other tasks such as sparse-view reconstruction, dynamic scene modeling, and geometry reconstruction. For instance, our experiments show that a straightforward per-splat texture mapping implementation similar to [Chao et al. 2024] does not yield consistent improvements beyond the dense view setup. In general, directly adding per-splat texture mapping suffers from two fundamental limitations. (1) The texture mapping lacks view- and time-dependent variations, which are essential for capturing specular reflections in novel view synthesis and temporal appearance variations in dynamic scene modeling. This shortcoming also hinders surface reconstruction, as the model may resort to incorrect geometry to compensate for insufficient view-dependent appearance modeling. (2) Locally optimizing perprimitive texture mappings can lead to redundant capacity and poor spatial consistency across neighboring splats, thereby increasing the risk of overfitting, as evidenced by the geometry reconstruction results in Table 1. This issue becomes particularly detrimental for both static and dynamic reconstruction under sparse-view settings, where global information is essential for robust optimization and improved generalization ability [Mihajlovic et al. 2024b].

To this end, we introduce Neural Texture Splatting (NTS), a unified framework that enhances 3DGS-based methods across a broad range of tasks. NTS augments each Gaussian primitive with local 2D or 3D RGBA texture fields to capture complex geometric and appearance variations. More importantly, we take inspiration from [Mihajlovic et al. 2024b] and leverage the implicit regularization of neural networks to enforce global consistency across primitives, thereby improving robustness and generalization across tasks, while also enabling efficient modeling of view- and time-dependent spatial variations within each splat. Specifically, we utilize a global tri-plane [Chan et al. 2022; Peng et al. 2020] and a neural network to decode each Gaussian primitive's local RGBA texture fields based on its position. The neural network can take both viewing direction

and timestep as inputs, hence producing view/time-dependent effects for local RGBA texture fields. During rendering, we adopt the ray-Gaussian intersection formula from [Yu et al. 2024d] to compute the 3D contribution point of each primitive, which is then used to query the local texture fields for additional color and opacity added to the original Gaussian splatting form of volume rendering.

Our contributions can be summarized as follows:

- We introduce Neural Texture Splatting (NTS), a novel representation that augments 3D Gaussian Splatting with neural per-primitive RGBA texture fields, serving as a robust representation that enhances 3DGS-based methods across a wide range of tasks.
- We propose to leverage a global tri-plane network to predict localized texture fields, enabling expressive modeling of geometry and appearance while ensuring robustness across tasks
- Extensive experiments demonstrate that our representation consistently improves existing state-of-the-art methods across diverse benchmarks, including dense and sparse-view novel view synthesis, surface reconstruction, and dynamic reconstruction.

2 Related Works

2.1 Novel View Synthesis

Recent advances in novel view synthesis (NVS) from calibrated multi-view images have introduced powerful scene representations, including multi-plane images [Broxton et al. 2020; Flynn et al. 2016; Zhou et al. 2018], voxel grids [Müller et al. 2022; Reiser et al. 2024; Sun et al. 2022], and neural fields [Mildenhall et al. 2020; Sitzmann et al. 2019]. Among these, 3D Gaussian Splatting (3DGS) [Kerbl et al. 2023] stands out as an efficient volumetric rendering approach that combines real-time rasterization with high-quality synthesis. Its flexibility has enabled extensions to surface [Huang et al. 2024; Yu et al. 2024d], sparse [Mihajlovic et al. 2024b], and dynamic scene reconstruction [Wu et al. 2024b; Yang et al. 2024a].

2.2 Splatting Beyond Gaussians

While 3DGS achieves remarkable efficiency and quality, its representational power is fundamentally limited by the fixed Gaussian kernel shape per splat. This restricts the model's ability to encode high-frequency details, fine geometry, and complex view-dependent effects. To address these limitations, recent works explore augmenting Gaussians with per-splat texture maps [Chao et al. 2024; Huang and Gong 2024; Rong et al. 2024; Song et al. 2024; Svitov et al. 2024; Xu et al. 2024a; Zhang et al. 2025a], introducing local 2D fields that modulate color and opacity. Texture-GS [Xu et al. 2024b] employs an explicit cubemap texture and a global 3D-to-2D mapping to achieve appearance editing. Others propose modifying the Gaussian kernel itself to better match surface geometry or appearance distributions [Li et al. 2025; Zhu et al. 2025].

Although these methods improve expressiveness for dense-input NVS, they often suffer from overfitting and lack robustness when generalized to sparse-view inputs, surface reconstruction, or dynamic scenes. In contrast, our Neural Texture Splatting (NTS) offers a unified and modular enhancement: we predict per-splat RGBA

texture fields using a shared global neural representation, allowing for efficient, view- and time-conditioned modeling. This approach substantially improves expressiveness and generalization, making NTS a plug-and-play upgrade to existing 3DGS pipelines across diverse tasks.

Surface Reconstruction

While the vanilla NeRF can be used to reconstruct surfaces, its resulting geometry is often noisy due to the lack of explicit regularization. A number of works have been proposed to improve the geometry reconstruction of NeRF, mainly by replacing the underlying density field with a geometrically regularized field, such as an occupancy field [Oechsle et al. 2021] or a signed distance field (SDF) [Li et al. 2023; Rosu and Behnke 2023; Wang et al. 2021, 2023; Yariv et al. 2021, 2023]. With the advent of 3DGS, a number of works have also been proposed to extend it to high-quality surface reconstruction. Initial efforts have focused on jointly optimizing a neural SDF with 3DGS, using the learned SDF to regularize the geometry of 3DGS [Chen et al. 2023; Yu et al. 2024c]. While effective, these methods suffer from slow optimization and excessive triangle counts when extracting the surface mesh. More recent works optimize only the Gaussian splatting parameters to maintain efficiency, while introducing additional regularization terms [Guédon and Lepetit 2024a; Huang et al. 2024; Turkulainen et al. 2024], novel re-parameterization of Gaussians [Dai et al. 2024a; Huang et al. 2024; Yu et al. 2024e], or advanced mesh extraction algorithms [Dai et al. 2024a; Guédon and Lepetit 2024a; Huang et al. 2024; Yu et al. 2024e] to achieve faithful surface reconstruction. Our proposed approach is compatible with these 3DGS surface reconstruction methods. We demonstrate the effectiveness of our approach by building on top of one of the latest methods [Yu et al. 2024e].

2.4 Sparse-view Static 3DGS Reconstruction

Recovering high-quality geometry and appearance from a small number of input views remains a major limitation for 3DGS, which typically relies on optimizing a large number of independent splats. This independence requires dense observations to constrain each primitive effectively, often leading to overfitting or poor generalization in sparse-view settings. Recent approaches tackle this issue by incorporating deep learned priors [Charatan et al. 2024; Chen et al. 2024; Chung et al. 2024; Tang et al. 2024; Zhang et al. 2025b]. In contrast, SplatFields [Mihajlovic et al. 2024b] avoids the sensitivity of such priors and introduces neural spatial regularization by regressing splat features from their 3D spatial positions. This induces a spatial autocorrelation bias that significantly improves performance in sparse-view scenarios. Our Neural Texture Splatting integrates seamlessly with SplatFields and further enhances reconstruction quality, as demonstrated in our experiments.

Sparse-view Dynamic 3DGS Reconstruction

Recent methods have extended Gaussian splatting to dynamic scenes by learning time-varying deformation fields with MLPs [Lu et al. 2024a; Wu et al. 2024c; Yang et al. 2023; Yu et al. 2024b]. However, these approaches typically rely on densely sampled views from

Table 1. Overfitting Issue for Per-primitive Texture Baseline. We use GOF [Yu et al. 2024d] as the backbone. Results on the DTU [Aanæs et al. 2016] dataset show that using a per-primitive texture representation without our proposed global neural texture is more prone to overfitting on training views, as evidenced by worse test Chamfer Distance (CD). In contrast, our global neural texture mitigates this issue and enhances generalization.

Method	Scan		Scan 1	
Wethou	Train PSNR↑	Test CD↓	Train PSNR↑	Test CD↓
W/o Neural Texture	36.05	0.48	39.42	0.70
W/ Neural Texture	34.73	0.44	38.99	0.64

varying camera positions to fully capture scene dynamics-an assumption that is rarely practical in real-world scenarios, where fixed camera rigs are commonly used to observe a scene from limited viewpoints. For a comprehensive overview of this growing area, we refer the reader to the recent survey on dynamic 3DGS [Fan et al. 2025].

To support dynamic reconstruction under sparse-view conditions, we build on SplatFields4D [Mihajlovic et al. 2024b], which employs the expressive ResFields architecture [Mihajlovic et al. 2024a] to model scene deformation from limited inputs. Our Neural Texture Splatting is fully compatible with this setup and further improves reconstruction quality, as shown in our experiments.

Background

3D Gaussian Splatting (3DGS) [Kerbl et al. 2023] represents scenes with a set of 3D Gaussian primitives, where each Gaussian primitive is defined by a 3D covariance matrix $\Sigma \in \mathbb{R}^{3 \times 3}$ and center position $\mu \in \mathbb{R}^3$. To ensure positive semi-definiteness, the covariance matrix is factorized into the rotation matrix $\mathbf{R} \in \mathbb{R}^{3\times3}$ and the scale matrix $S \in \mathbb{R}^{3 \times 3}$ as $\Sigma = RSS^TR^T$. The 3D Gaussian kernel of the k-th primitive, denoted as G_k , is defined as:

$$\mathcal{G}_k(\mathbf{x}) = \exp(-\frac{1}{2}(\mathbf{x} - \mu_k)^T \Sigma_k^{-1}(\mathbf{x} - \mu_k))$$
s.t. $\Sigma_k = \mathbf{R}_k \mathbf{S}_k \mathbf{S}_k^{\mathsf{T}} \mathbf{R}_k^{\mathsf{T}}$ (1)

To differentially render the color of a pixel $\mathbf{p} \in \mathbb{R}^2$, the colors associated with Gaussian primitives are alpha-composited from front to back, following the conventional volume rendering equation:

$$\mathbf{c}(\mathbf{p}) = \sum_{k=1}^{K} \mathbf{c}_k \alpha_k \mathcal{P}(\mathcal{G}_k, \mathbf{p}) \prod_{j=1}^{k-1} (1 - \alpha_k \mathcal{P}(\mathcal{G}_k, \mathbf{p}))$$
(2)

where $\mathbf{c}_k \in \mathbb{R}^3$, $\alpha_k \in [0, 1]$ are the view-dependent color and opacity of the primitive, respectively. $\mathcal{P}(\mathcal{G}_k, \mathbf{p})$ evaluates the 3D Gaussian kernel G_k to the camera ray corresponding to the pixel **p**. This evaluation can be done by either EWA splatting [Zwicker et al. 2002], exact projection of 2D surfels [Huang et al. 2024], or finding the ray-primitive intersection [Yu et al. 2024e]. The attributes of the Gaussians, including their center position, rotation, scale, opacity, and color (modeled using spherical harmonic coefficients to account for view-dependent effects), are optimized through gradient descent by minimizing photometric losses computed on the rendered 2D images.

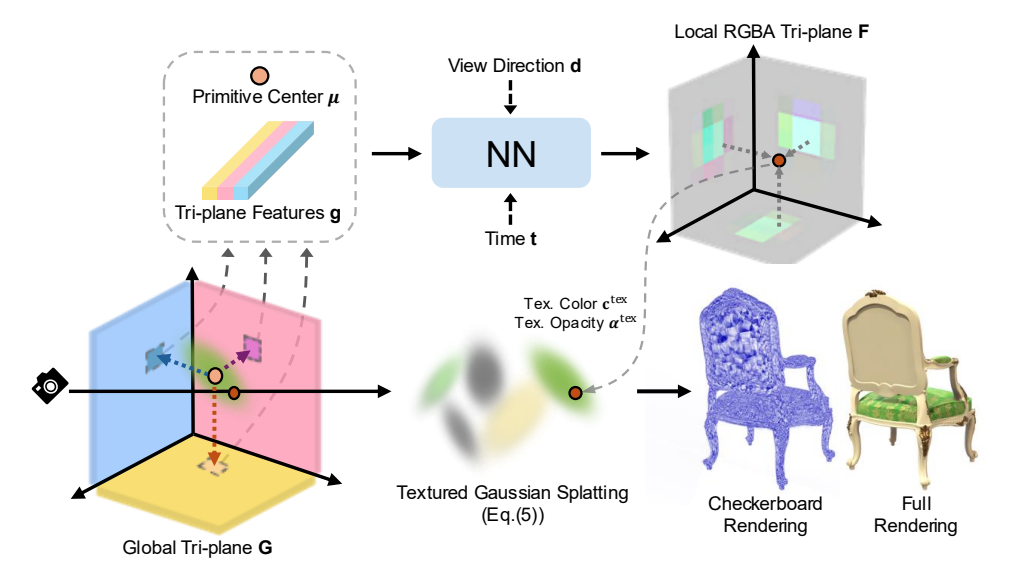


Fig. 2. **Method Overview**. Our method enhance 3D Gaussian Splatting (3DGS) by introducing a local RGBA tri-plane texture to each splat (top right). During rendering with our proposed textured Gaussian Splatting (bottom, Sec. 4.1), each ray computes the intersection point with splats and queries the corresponding RGBA textures, which are combined with the original Gaussian attributes to produce the final rendering result via volume rendering (Eq.(5)). We show checkerboard and learned RGB texture renderings for visualization. While this local texture field improves the representational capacity of color and opacity, it also increases the risk of overfitting and lacks the ability to capture view- and time-dependent variations. To address these limitations, we introduce a global tri-plane neural field that models the local texture fields in a compact and shared manner (top, Sec. 4.2).

4 Methods

In this section, we describe our method in detail (illustrated in Fig. 2).

4.1 Textured Gaussian Splatting

The expressiveness of the 3DGS primitive (hereafter referred to as *splat*) is inherently limited, as it models color and opacity distributions using a single 3D Gaussian kernel. However, real-world scenarios often exhibit significantly more complex spatial variations in both geometry and appearance, such as high-frequency view-dependent effects. In this work, we introduce a learnable RGBA texture field for each splat, complementing the original Gaussian kernel \mathcal{G}_k , to more effectively capture detailed local variations in appearance and geometry.

We define the RGBA texture field \mathcal{F} in the local coordinate system of each splat. Given a world space point $\hat{\mathbf{x}}$, its corresponding point $\mathbf{x}_k = \{x_k, y_k, z_k\}$ in the local coordinate of the kth splat is calculated using the splat's center position $\boldsymbol{\mu}_k$, scale matrix \mathbf{S}_k and rotation matrix \mathbf{R}_k as

$$\mathbf{x}_k = \mathbf{S}_k^{-1} \mathbf{R}_k (\hat{\mathbf{x}} - \boldsymbol{\mu}_k) \tag{3}$$

The RGBA texture values of $\mathbf{c}_k^{\mathrm{tex}}(\hat{\mathbf{x}})$ and $\alpha_k^{\mathrm{tex}}(\hat{\mathbf{x}})$, for the world point $\hat{\mathbf{x}}$, are queried from the texture field \mathcal{F} using the local coordinate point \mathbf{x}_k as

$$\mathbf{c}_k^{\text{tex}}(\hat{\mathbf{x}}), \alpha_k^{\text{tex}}(\hat{\mathbf{x}}) = \mathcal{F}(\mathbf{x}_k)$$
 (4)

We interpret the queried RGBA texture values $\mathbf{c}_k^{\mathrm{tex}}(\hat{\mathbf{x}})$ and $a_k^{\mathrm{tex}}(\hat{\mathbf{x}})$ as approximations of the integrated contributions from the entire local texture field during volume rendering. These contributions are added to the original color and opacity terms in the standard rendering formulation of conventional Gaussian Splatting (Eq.(2)), enhancing its expressiveness. Accordingly, we define the modified

volume rendering equation for our Textured Gaussian Splatting as follows:

$$\mathbf{c}(\mathbf{p}) = \sum_{k=1}^{K} (\mathbf{c}_{k} + \mathbf{c}_{k}^{\text{tex}}(\hat{\mathbf{x}}_{k}))(\alpha_{k} \mathcal{P}(\mathcal{G}_{k}, \mathbf{p}) + \alpha_{k}^{\text{tex}}(\hat{\mathbf{x}}_{k})) \cdot \prod_{j=1}^{K-1} \left(1 - \alpha_{j} \mathcal{P}(\mathcal{G}_{j}, \mathbf{p}) - \alpha_{j}^{\text{tex}}(\hat{\mathbf{x}}_{j})\right)$$
(5)

Here, $\hat{\mathbf{x}}_k$ denotes the query point used to evaluate the RGBA texture field \mathcal{F} for the k-th Gaussian primitive. The opacity term in volume rendering, $\alpha_k \mathcal{P}(\mathcal{G}_k, \mathbf{p}) + \alpha_k^{\text{tex}}(\hat{\mathbf{x}}_k)$, is clamped to [0, 0.99] to ensure that the resulting transmittance remains non-negative. We adopt the ray–Gaussian intersection algorithm in [Yu et al. 2024e] to obtain the query point for the RGBA texture field. Since the integrated texture value is primarily learned through the RGBA texture fields, our representation remains compatible with alternative ray–Gaussian intersection algorithms [Chao et al. 2024; Huang and Gong 2024].

Modeling the RGBA Texture Field. Instead of employing a continuous implicit representation, such as a small MLP [Reiser et al. 2021], for each local texture field, we adopt an explicit representation to improve computational efficiency. We use a fixed resolution τ to discretize the RGBA texture field \mathcal{F} . While a straightforward approach would be to represent it using a $\tau \times \tau \times \tau$ voxel grid, we found this to be memory-inefficient, especially at higher resolutions. This motivates us to employ a tri-plane representation [Chan et al. 2022; Chen et al. 2022; Peng et al. 2020] to compress the RGBA volume.

Specifically, the RGBA volume of the k-th splat is represented by three orthogonal learnable planes, \mathbf{F}_{xy}^k , \mathbf{F}_{xz}^k , and \mathbf{F}_{yz}^k , each in $\mathbb{R}^{\tau \times \tau \times 4}$. Each plane has a resolution of $\tau \times \tau$ and stores 4-channel RGBA values. Given a point in the splat's local coordinate $\mathbf{x}_k = \{x_k, y_k, z_k\}$,

its corresponding local color and opacity values can be obtained by querying the three planes:

$$\begin{aligned} \mathbf{f}_{xy}^{k}(\mathbf{x}_{k}) &= \mathbf{F}_{xy}^{k}(x_{k}, y_{k}) \\ \mathbf{f}_{xz}^{k}(\mathbf{x}_{k}) &= \mathbf{F}_{xz}^{k}(x_{k}, z_{k}) \\ \mathbf{f}_{yz}^{k}(\mathbf{x}_{k}) &= \mathbf{F}_{yz}^{k}(y_{k}, z_{k}) \\ \mathbf{c}_{k}^{\text{tex}}(\mathbf{x}_{k}), \alpha_{k}^{\text{tex}}(\mathbf{x}_{k}) &= \frac{1}{3} (\mathbf{f}_{xy}^{k}(\mathbf{x}_{k}) + \mathbf{f}_{xz}^{k}(\mathbf{x}_{k}) + \mathbf{f}_{yz}^{k}(\mathbf{x}_{k})) \end{aligned} \tag{6}$$

We employ bilinear interpolation when sampling from each of the three planes and discard query points outside a local bounding box of size 3. An alternative approach, which approximates the texture field using a 2D RGBA texture, is described in the supplementary material.

4.2 **Neural Texture Splatting**

While the local RGBA textures capture spatial variations of color and opacity within a splat, these variations are view-independent and time-independent, making them suboptimal for modeling complex view-dependent effects and temporal dynamics. Furthermore, persplat RGBA textures often introduce redundant representational capacity and lack spatial consistency across neighboring splats, resulting in reduced generalization and robustness. We observe that directly optimizing these textures yields limited improvements across tasks: although they result in noticeable gains for novel view synthesis, their effectiveness degrades significantly in other scenarios, such as surface reconstruction and sparse-view reconstruction, as demonstrated in Table 1.

To address this issue, we propose using a global neural field to model local texture fields in a compact and shared manner, enabling information sharing to achieve robust optimization. We begin by leveraging a global tri-plane representation, denoted as $G_{xy}, G_{xz}, G_{yz} \in \mathbb{R}^{H \times W \times C}$, to encode features $g_k \in \mathbb{R}^C$ for the k-th splat. For each splat, the global tri-plane features \mathbf{g}_k are extracted at its center position $\mu_k = (\mu_x, \mu_y, \mu_z)$ as follows:

$$\begin{aligned} \mathbf{g}_{xy}^{k} &= \mathbf{G}_{xy}(\mu_{x}^{k}, \mu_{y}^{k}), \quad \mathbf{g}_{xz}^{k} &= \mathbf{G}_{xz}(\mu_{x}^{k}, \mu_{z}^{k}), \quad \mathbf{g}_{yz}^{k} &= \mathbf{G}_{yz}(\mu_{y}^{k}, \mu_{z}^{k}), \\ \mathbf{g}_{k} &= \mathrm{Concat}(\mathbf{g}_{xy}^{k}, \mathbf{g}_{xz}^{k}, \mathbf{g}_{yz}^{k}). \end{aligned} \tag{7}$$

The global tri-plane features \mathbf{g}_k are concatenated with the splat's center position μ_k and additional attributes, such as the viewing direction \mathbf{d}_k , and an optional time step \mathbf{t} for dynamic scenes. The combined feature is then passed through a shallow global neural network to predict the RGBA volume, represented by the local RGBA tri-planes textures F_{xy}^k , F_{xz}^k , and F_{yz}^k for the k-th splat.

$$\{\mathbf{F}_{xy}^{k}, \mathbf{F}_{xz}^{k}, \mathbf{F}_{yz}^{k}\} = \text{NN}(\mathbf{g}_{k}, \boldsymbol{\mu}_{k}, \mathbf{d}_{k}, \mathbf{t})$$
(8)

where t is included only for dynamic scenes and omitted for static ones. We employ distinct global triplanes G and Neural decoders NN for color and opacity textures. The view direction serves as input only to the color network.

While the neural network could directly predict the RGBA triplane textures with a total dimension of $\tau \times \tau \times 3 \times 4$, we wish to further reduce computational cost and enable the use of higherresolution local texture planes. To this end, we utilize Canonical Polyadic (CP) decomposition to represent each of the three local

Table 2. Dynamic Reconstruction. We report averaged metrics on the Owlii dataset with 4, 6, 8 and 10 training views. Detailed breakdowns are shown in Fig. 5 and in the appendix tables. SSIM/LPIPS values are scaled by 100 for clarity. 1st, 2nd and 3rd denote the best results.

Method	Mean	Dancer	PSNR ↑ Exercise	Model	Basketball
4D-GS	23.27	23.92	23.27	24.11	21.78
Deformable3DGS	24.58	25.36	24.72	23.98	24.26
4DGaussians	26.45	25.86	26.41	27.38	26.15
SplatFields4D	27.87	28.16	27.16	28.02	28.13
SplatFields4D + Ours	29.25	29.54	28.74	29.21	29.50
			SSIM ↑		
	Mean	Dancer	Exercise	Model	Basketball
4D-GS	88.81	89.96	88.92	87.87	88.48
Deformable3DGS	91.05	92.03	91.88	89.02	91.29
4DGaussians	93.57	93.38	94.26	92.79	93.86
SplatFields4D	95.09	95.49	95.24	93.99	95.66
SplatFields4D + Ours	95.86	96.28	95.91	94.97	96.28
			LPIPS ↓		
	Mean	Dancer	Exercise	Model	Basketball
SplatFields4D	7.18	6.78	7.74	7.84	6.38
SplatFields4D + Ours	6.70	6.10	7.42	7.17	6.08

planes. Specifically, the network outputs 1D vectors that produce planes via outer products. For the k-th splat, the neural network predicts a pair of RGBA vectors $\mathbf{v}_{uv}^{0,k} \in \mathbb{R}^{4\tau}$ and $\mathbf{v}_{uv}^{1,k} \in \mathbb{R}^{4\tau}$ for each plane $uv \in \{xy, xz, yz\}$. Each local RGBA tri-plane texture is then computed as the outer product of the corresponding vector pair:

$$\{\mathbf{v}_{xy}^{0,k}, \mathbf{v}_{xy}^{1,k}, \mathbf{v}_{xz}^{0,k}, \mathbf{v}_{yz}^{1,k}, \mathbf{v}_{yz}^{0,k}, \mathbf{v}_{yz}^{1,k}\} = \text{NN}(\mathbf{g}_k, \mathbf{R}_k, \boldsymbol{\mu}_k, \mathbf{r}, t),$$

$$\mathbf{F}_{xy}^k = \mathbf{v}_{xy}^{0,k} \otimes \mathbf{v}_{xy}^{1,k}, \quad \mathbf{F}_{xz}^k = \mathbf{v}_{xz}^{0,k} \otimes \mathbf{v}_{xz}^{1,k}, \quad \mathbf{F}_{yz}^k = \mathbf{v}_{yz}^{0,k} \otimes \mathbf{v}_{yz}^{1,k}.$$

$$(9)$$

4.3 Optimization

We adopt the original optimization objective of 3DGS, e.g., a combination of L1 distance and D-SSIM term as

$$\mathcal{L}_{c} = \mathcal{L}_{\text{MSE}}(\hat{I}, I) + \lambda \mathcal{L}_{\text{D-SSIM}}(\hat{I}, I)$$
 (10)

where \hat{I} denotes ground-truth target image and I the corresponding rendered target image. We set $\lambda = 0.2$, and when integrating with other baselines such as GOF [Yu et al. 2024d], we retain the auxiliary loss terms as defined in their original implementations.

In addition, we introduce an L1 regularization term on the triplane RGBA textures to encourage sparsity:

$$\mathcal{L}_{\text{norm}} = \frac{1}{N \cdot \tau^2} \sum_{u,v} (\| \mathbf{F}_{xy}(u,v) \| + \| \mathbf{F}_{xz}(u,v) \| + \| \mathbf{F}_{yz}(u,v) \|)$$
 (11)

where N is the number of splats, τ denotes the resolution of each texture plane, and (u, v) refers to the grid coordinates on the texture planes. $\mathcal{L}_{\text{norm}}$ is combined with \mathcal{L}_c using a loss weight of 0.01. A detailed ablation study of the components and hyperparameters is shown in Table 9.

Table 3. **Sparse-view Reconstruction**. We report averaged metrics on the Blender dataset with 4, 6, 8 and 10 training views. Detailed breakdowns are shown in Fig. 4 and in the appendix tables. SSIM/LPIPS values are scaled by 100 for clarity. 1st, 2nd and 3rd denote the best results.

Method					PSNR	1			
Wethou	Mean	Toy	Ficus	Hotdog	Chair	Mic	Ship	Drums	Materials
SparseNeRF	20.88	22.47	17.96	26.01	23.61	19.64	20.16	16.76	20.42
SuGaR	19.43	20.39	21.16	21.69	22.14	18.07	18.22	17.34	16.47
ScaffoldGS	20.17	19.14	21.08	21.23	21.88	24.75	17.61	17.77	17.89
Mip-Splatting	20.75	20.29	22.40	21.55	22.04	24.75	18.24	18.49	18.23
3DGS	21.26	20.65	22.80	22.88	22.80	25.43	18.71	18.63	18.16
LightGaussian	21.41	20.95	23.85	22.41	22.99	25.12	18.98	18.81	18.21
2DGS	21.44	20.49	22.61	24.80	23.77	24.86	18.34	18.73	17.96
SplatFields3D	22.58	23.13	23.00	26.66	23.98	25.11	20.36	19.57	18.87
$SplatFields 3D + {\bf Ours}$	23.05	23.74	23.02	26.87	24.18	25.71	21.14	20.01	19.77
	SSIM↑								
	Mean	Toy	Ficus	Hotdog	Chair	Mic	Ship	Drums	Materials
SparseNeRF	84.08	85.30	82.95	92.70	87.81	86.87	73.76	78.76	84.52
SuGaR	80.51	79.01	86.27	87.51	85.50	84.05	69.86	76.92	74.92
ScaffoldGS	81.10	76.50	87.52	84.60	84.34	93.53	65.31	78.69	78.32
Mip-Splatting	83.75	79.44	89.81	88.02	86.75	94.55	68.37	82.68	80.38
3DGS	84.15	80.27	90.24	88.85	87.64	94.71	68.40	83.09	79.95
LightGaussian	84.90	81.08	91.46	89.63	87.82	94.76	69.36	83.67	81.40
2DGS	85.23	81.15	90.28	90.97	88.94	94.68	70.70	84.35	80.78
SplatFields3D	87.04	85.41	90.28	93.87	88.86	94.46	75.89	85.51	82.01
SplatFields3D + Ours	87.70	86.00	90.67	93.99	89.08	94.80	77.12	86.21	83.70
					LPIPS	1			
	Mean	Toy	Ficus	Hotdog	Chair	Mic	Ship	Drums	Materials
SplatFields3D	13.49	13.86	8.97	9.23	11.63	5.62	28.07	13.06	17.44
SplatFields3D + Ours	13.50	14.03	8.22	9.55	11.89	5.46	28.75	12.92	17.20

5 Experiments

In this section, we demonstrate the effectiveness of our approach by integrating it into several state-of-the-art 3D Gaussian Splatting (3DGS) variants and evaluating its performance across a diverse set of reconstruction tasks.

5.1 Setup

Datasets. Our evaluation spans multiple standard benchmarks. We first benchmark sparse-view reconstruction on the Blender dataset [Mildenhall et al. 2020] and the Owlii dataset [Xu et al. 2017] for static and dynamic scenes, respectively. We then evaluate surface reconstruction on the DTU dataset [Aanæs et al. 2016] and dense-view novel view synthesis on the Blender [Mildenhall et al. 2020] and Mip-NeRF360 [Barron et al. 2022] datasets. We use standard metrics for novel view synthesis, including PSNR, SSIM [Wang et al. 2004], and LPIPS [Zhang et al. 2018]. For surface reconstruction, we measure geometric accuracy using Chamfer Distance on the extracted mesh, following [Huang et al. 2024; Yu et al. 2024d].

Backbone choice. We adopt GOF [Yu et al. 2024d] and 3DGS-MCMC [Kheradmand et al. 2024] for dense-view reconstruction tasks, and employ SplatFields [Mihajlovic et al. 2024b] as our backbone model for sparse-view scenarios. Each of these methods demonstrates state-of-the-art performance in different domains: GOF excels in surface reconstruction, 3DGS-MCMC in dense-view novel view synthesis, and SplatFields in sparse-view 3D reconstruction and dynamic 4D scene modeling.

Table 4. **Dense-view Reconstruction**. Our method consistently improves the performance of both Gaussian Opacity Field (GOF) and 3DGS-MCMC across novel view synthesis and surface reconstruction tasks.

Method		Blender		M	lipNeRF3	60	DTU
Method	PSNR↑	SSIM↑	LPIPS↓	PSNR↑	SSIM↑	LPIPS↓	$CD\downarrow$
MipNeRF360	30.34	0.9510	0.0600	27.69	0.7920	0.2370	
Instant-NGP	32.20	0.9590	0.0550	25.30	0.6710	0.3710	
3DGS	33.08	0.9671	0.0440	27.26	0.8318	0.1871	
TexturedGaussians	33.24	0.9674	0.0428	27.35	0.8274	0.1858	
2DGS	33.08	0.9680	0.0332	26.81	0.7967	0.2520	0.80
GOF	33.44	0.9698	0.0307	27.45	0.8272	0.1945	0.74
GOF + Ours	34.09	0.9710	0.0286	27.71	0.8257	0.1964	0.67
3DGS-MCMC	33.81	0.9718	0.0284	28.14	0.8427	0.1755	
3DGS-MCMC + Ours	34.06	0.9724	0.0275	28.24	0.8429	0.1748	

5.2 Sparse-view Scene Reconstruction

We demonstrate that our model significantly enhances representational expressiveness while maintaining strong generalization under sparse-view settings, outperforming the current state-of-theart method [Mihajlovic et al. 2024b] in reconstructing both static and dynamic scenes. Comprehensive benchmark results and additional qualitative visualizations are provided in the supplementary document and accompanying video.

Static Scene. We compare our method against recent 3DGS [Fan et al. 2023; Guédon and Lepetit 2024b; Huang et al. 2024; Kerbl et al. 2023; Lu et al. 2024b; Mihajlovic et al. 2024b; Yu et al. 2024a] and NeRF-based [Guangcong et al. 2023] approaches for sparseview static scene reconstruction. Following the SplatFields protocol, we conduct experiments on the Blender dataset [Mildenhall et al. 2020], varying the number of training views from 4 to 10. Table 3 presents a comprehensive comparison averaged over the 4, 6, 8, and 10-view settings, where our method achieves the best performance among the baselines. As shown in Fig. 4, which illustrates the performance of SplatFields, SplatFields+Ours, and 3DGS with respect to the number of input views, our method consistently outperforms the state-of-the-art SplatFields across varying view counts. Qualitative comparison between ours and SplatFields under the 10-view input setting are presented in Fig. 10, where our method produces sharper reconstructions with fewer floater artifacts.

Dynamic Scene. To evaluate dynamic scene reconstruction under real-world conditions, we adopt four sequences from the Owlii dataset [Xu et al. 2017] as benchmarks. We use 100 frames for training and 100 test frames captured from varying viewpoints along a rotating camera trajectory. We compare our method with recent dynamic 3D Gaussian Splatting approaches – 4D-GS [Yang et al. 2024b], Deformable3DGS [Yang et al. 2024a], and 4DGaussians [Wu et al. 2024b] – under varying numbers of input views, ranging from 4 to 10. Complete benchmark results and additional comparisons with dynamic NeRF methods [Li et al. 2022; Park et al. 2021a,b; Pumarola et al. 2021] are provided in the supplementary material.

Quantitative results averaged over the 4, 6, 8, and 10-view input settings are reported in Table 2. Fig. 5 further shows performance trends as the number of input views increases from 4 to 10,

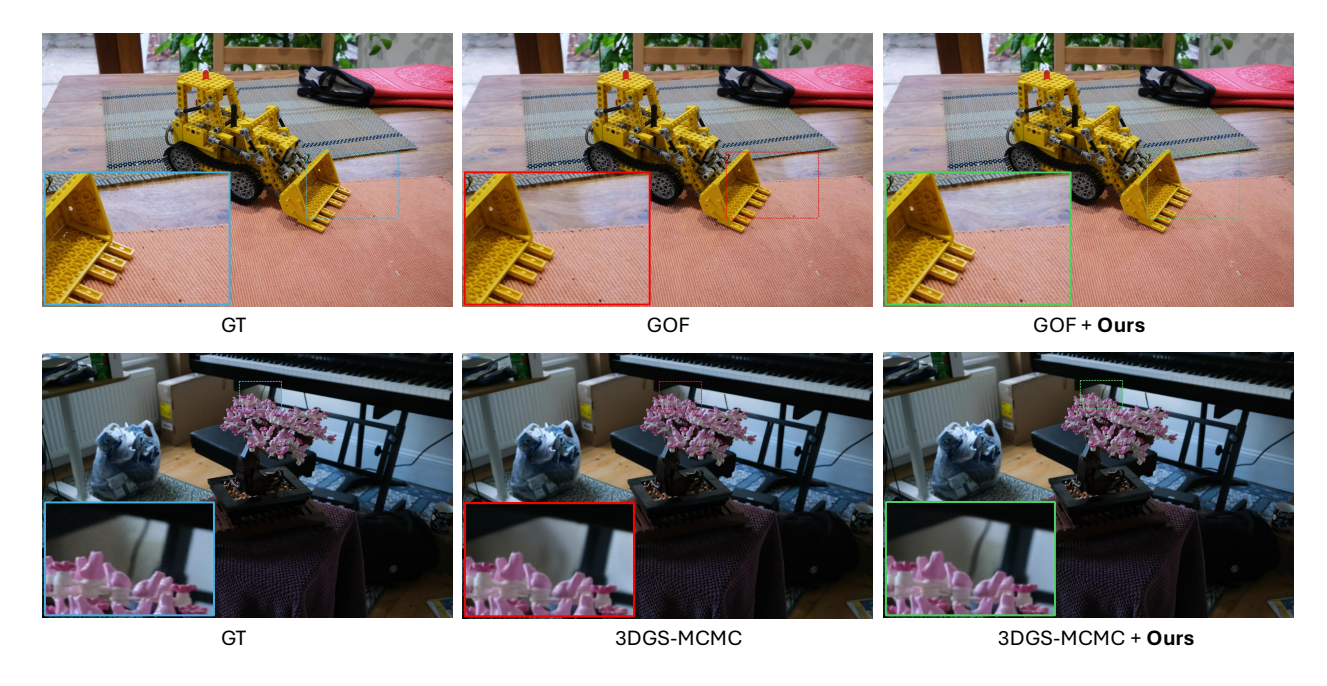


Fig. 3. Qualitative comparison of novel view synthesis on the MipNeRF360 dataset. Our method enhances baselines by better handling view-dependent effects and preserving fine-grained structures.

Table 5. Efficiency Benchmark. Comparison of baseline methods (3DSG-MCMC, SplatFields) and our variants across reconstruction quality (PSNR), number of Gaussians (#G), model size, training VRAM, training time, and rendering FPS.

Dataset	Method	PSNR	#G	Size	VRAM	Time	FPS
Blender	3DSG-MCMC	33.81	0.29M	69MB	6GB	5min	380
	3DSG-MCMC + Ours	34.06	0.29M	87MB	15GB	36min	85
MipNeRF360	3DSG-MCMC	28.14	3.56M	842MB	15GB	15min	135
	3DSG-MCMC + Ours	28.24	3.56M	860MB	43GB	75min	37
Blender	SplatFields	22.58	0.30M	74MB	8GB	80min	430
	SplatFields + Ours	23.05	0.33M	86MB	17GB	135min	150
Owlii	SplatFields	27.87	0.10M	28MB	7GB	14h	38
	SplatFields + Ours	29.25	0.10M	31MB	11GB	23h	15

comparing SplatFields, SplatFields+Ours, and the second-best baseline, 4DGaussians. Across all view counts, our method consistently achieves superior performance.

Fig. 6 demonstrates that under the challenging sparse-view setup, our method effectively mitigates floaters and boundary artifacts. With 10 input views, as illustrated in Fig. 7, our approach yields qualitatively superior reconstructions, recovering fine-grained details and producing sharper, more geometrically faithful structures, particularly in challenging regions such as human faces and hands.

Dense-view Scene Reconstruction

We evaluate our model's effectiveness in dense-view reconstruction on both synthetic and real-world benchmarks. For comparison, the 3DGS-based methods are trained for 30k iterations. In our setup, we first pretrain our backbone model for 5k iterations and then jointly train with our module for an additional 25k iterations, using the same hyperparameters throughout to ensure a fair comparison.

Novel View Synthesis. We evaluate the effectiveness of our method in enhancing novel view synthesis by integrating it with two stateof-the-art baselines, GOF [Yu et al. 2024d] and 3DGS-MCMC [Kheradmand et al. 2024]. Experiments are conducted on both the synthetic Blender dataset [Mildenhall et al. 2020] and the real-world MipNeRF360 dataset [Barron et al. 2021]. As shown in Table 4, our approach consistently improves the performance of both baselines across both benchmarks, with particularly notable gains in PSNR. Moreover, our variants of existing 3DGS methods achieve the best performance among prior works [Barron et al. 2022; Chao et al. 2024; Huang et al. 2024; Kerbl et al. 2023; Müller et al. 2022]. Qualitative results are presented in Fig. 9 and Fig. 3, where our method enhances the baselines' ability to capture high-frequency, view-dependent effects such as specular highlights. Moreover, it effectively preserves fine-grained structures (e.g., the cable shown in the figure) that are often missed by baseline methods due to their limited local expressiveness.

Surface Reconstruction. We further validate our model's ability to recover more accurate surfaces by building upon the state-ofthe-art 3DGS-based surface reconstruction method, GOF [Yu et al. 2024d]. As benchmarked on the DTU [Aanæs et al. 2016] dataset and shown in Table 4, our approach demonstrates improved surface reconstruction performance compared to the original method. A detailed per-scene breakdown and additional baseline comparisons are provided in the appendix. Qualitative results in Fig. 8 demonstrate that our model produces more accurate and smoother surfaces, benefiting from the enhanced local expressiveness of Gaussian primitives for both geometry and appearance. Additionally, our ability to model view-dependent effects is particularly effective in recovering

Table 6. **Breakdown of Inference Time on Blender Dataset.** We report average runtimes (ms) of each component when rendering a single 800×800 image from 0.3M primitives. Compared to vanilla 3DGS (Rasterization only), the additional computational overhead in our method is primarily due to the ray-Gaussian intersection and Neural Network (NN) forward pass.

Component	Rasterization	Ray-Gaussian Intersection	Texture Query	NN Forward
Time (ms)	2.6	4.2	0.2	4.7

Table 7. **Ablation Studies on Model Variants.** We ablate the effect of removing the global neural network (w/o Neural) and report the performance of our model at the same model size (Ours (Full) †) as the baselines.

Method	Blender PSNR↑	(100 views) SSIM↑	Blender PSNR↑		Owlii (4 PSNR↑	4 views) SSIM↑	DTU CD↓
Baseline	33.44	0.9698	19.16	0.8227	21.95	0.9160	0.74
+ Ours (w/o Neural)	33.63	0.9696	19.14	0.8144	22.64	0.9072	0.72
+ Ours (Full) [†]	34.00	0.9721	20.00	0.8350	25.01	0.9308	0.68
+ Ours (Full)	34.09	0.9710	19.98	0.8351	25.05	0.9319	0.67

specular surface regions with fewer holes, as shown in the *apple* example.

5.4 Efficiency Analysis

We present a comprehensive efficiency analysis by reporting averaged results for baseline methods (3DGS-MCMC [Kheradmand et al. 2024], SplatFields [Mihajlovic et al. 2024b]) and our variants across datasets. Table 5 summarizes the efficiency statistics, including reconstruction quality measured in PSNR, the number of Gaussians, model size, training GPU memory (VRAM), training time, and rendering FPS. Under the same number of primitives, our method maintains a comparable model size thanks to the global neural network, which effectively compresses per-primitive local RGBA textures. The increase in training GPU memory primarily arises from storing RGBA texture gradients, while the forward rendering stage introduces approximately 1 GB of additional memory usage for millions of primitives. As detailed in Table 6, the reduction in rendering FPS mainly stems from the ray-Gaussian intersection algorithm adopted from GOF [Yu et al. 2024d] and the forward pass of the global neural network. Despite the additional overhead, our method achieves superior reconstruction quality and consistently outperforms the baselines at the same model size (see Ours (Full)† in Table 7).

5.5 Ablation Studies

Effect of Global Neural Network. We first ablate our key idea of using a global neural network to model local texture fields, as shown in Table 7. Compared to naive per-primitive RGBA textures (refer to w/o Neural in the table), our neural texture splatting method achieves significant and consistent improvements across all evaluated benchmarks. In particular, our method achieves notable gains of approximately 3 dB in PSNR for dynamic scene reconstruction on the Owlii (4 views) dataset. This improvement is primarily attributed to the ability of our neural texture modeling to capture time-dependent texture variations, a crucial capability that per-primitive RGBA textures lack.

Table 8. Effectiveness of Local RGBA Texture. We compare against variants where the global neural network predicts per-primitive RGB values or spherical harmonics with an additional alpha channel. Our local RGBA texture representation yields consistently better meterics across datasets and backbones (GOF for Blender, 3DGS-MCMC for MipNeRF360).

	Blender				MipNeRF360			
Method	PSNR↑	SSIM↑	LPIPS↓	PSNR↑	SSIM↑	LPIPS↓		
Baseline	33.44	0.9698	0.0307	28.14	0.8427	0.1755		
+ Neural RGBA	33.79	0.9703	0.0300	28.17	0.8413	0.1799		
+ Neural SHA	33.85	0.9703	0.0296	28.20	0.8415	0.1806		
+ Ours	34.09	0.9710	0.0286	28.24	0.8429	0.1748		

Table 9. **Ablation Studies on Method Components and Hyperparameters.** We evaluate the impact of different components and hyperparameters on the Blender dataset with GOF as the backbone.

Method	PSNR↑	SSIM↑	LPIPS↓	Model Size (MB)
Ours	34.09	0.9710	0.0286	68.2
W/o CP Decomposition	34.03	0.9708	0.0284	75.1
W/o Sparsity Loss	34.09	0.9708	0.0287	73.2
W/o View-dependence	33.74	0.9704	0.0293	68.5
W/ Tri-plane Resolution 128	34.08	0.9710	0.0286	63.1
W/ Tri-plane Resolution 256	34.00	0.9708	0.0287	77.7
W/ NN Depth 3	34.03	0.9710	0.0286	68.5
W/ NN Width 256	34.06	0.9709	0.0287	68.9

Effect of Local RGBA Textures. The variant w/o Neural in Table 7 shows that our local RGBA texture representation can improve baseline performance across all benchmarks without relying on a global neural network. To further assess its effectiveness, we compare against variants where the global neural network predicts per-primitive RGB values or spherical harmonics augmented with an alpha channel (denoted as Neural RGBA and Neural SHA in Table 8). Our local texture fields consistently demonstrate superior results across datasets and backbones, using GOF as the baseline on Blender and 3DGS-MCMC on MipNeRF360.

Components and Hyperparameters. Table 9 reports ablation studies on our method's components and hyperparameters on the Blender dataset, with GOF as the backbone. The inclusion of CP decomposition (Eq.(9)) and sparsity loss (Eq.(11)) help reduces model size, and view-dependent texture representation improves reconstruction quality. The results also show that our design choices consistently maintain high reconstruction quality across different architectural variations, such as global tri-plane resolution and neural network depth/width.

6 Conclusion

We have proposed Neural Texture Splatting (NTS), a novel extension for 3D Gaussian Splatting (3DGS) to enhance its local expressiveness and generalization ability. We have demonstrated that NTS is most effective when tackling the sparse-view reconstruction problem, where it significantly improves the quality of both static and dynamic scene reconstruction. We have also shown that NTS can be easily integrated into other 3DGS frameworks, such as geometry

reconstruction [Yu et al. 2024e] and dense-view novel view synthesis [Kheradmand et al. 2024], achieving noticeable improvements over the state-of-the-art on these tasks. Despite the improved reconstruction quality, future work could focus on enhancing computational efficiency, for example through more efficient ray-Gaussian intersection algorithms [Bulo et al. 2025] and faster neural architectures [Müller et al. 2022]. We believe that NTS is a promising step towards a more expressive 3DGS framework, and we hope that it will inspire further research in this direction.

Acknowledgments

We would like to express our gratitude to Brian Chao and Qin Han for their helpful discussions.

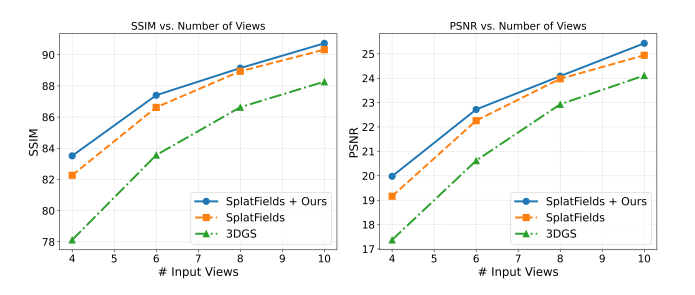
References

- Henrik Aanæs, Rasmus Ramsbøl Jensen, George Vogiatzis, Engin Tola, and Anders Bjorholm Dahl. 2016. Large-Scale Data for Multiple-View Stereopsis. International Journal of Computer Vision (2016), 1-16.
- Jonathan T Barron, Ben Mildenhall, Matthew Tancik, Peter Hedman, Ricardo Martin-Brualla, and Pratul P Srinivasan. 2021. Mip-nerf: A multiscale representation for anti-aliasing neural radiance fields. In Proceedings of the IEEE/CVF international conference on computer vision. 5855-5864.
- Jonathan T. Barron, Ben Mildenhall, Dor Verbin, Pratul P. Srinivasan, and Peter Hedman. 2022. Mip-NeRF 360: Unbounded Anti-Aliased Neural Radiance Fields. CVPR (2022).
- Michael Broxton, John Flynn, Ryan Overbeck, Daniel Erickson, Peter Hedman, Matthew Duvall, Jason Dourgarian, Jay Busch, Matt Whalen, and Paul Debevec. 2020. Immersive light field video with a layered mesh representation. ACM Transactions on Graphics (TOG) 39, 4 (2020), 86-1.
- Samuel Rota Bulo, Nemanja Bartolovic, Lorenzo Porzi, and Peter Kontschieder. 2025. Hardware-Rasterized Ray-Based Gaussian Splatting. In Proceedings of the Computer Vision and Pattern Recognition Conference. 485-494.
- Eric R. Chan, Connor Z. Lin, Matthew A. Chan, Koki Nagano, Boxiao Pan, Shalini De Mello, Orazio Gallo, Leonidas Guibas, Jonathan Tremblay, Sameh Khamis, Tero Karras, and Gordon Wetzstein. 2022. Efficient Geometry-aware 3D Generative Adversarial Networks. In IEEE Conf. Comput. Vis. Pattern Recog.
- Brian Chao, Hung-Yu Tseng, Lorenzo Porzi, Chen Gao, Tuotuo Li, Qinbo Li, Ayush Saraf, Jia-Bin Huang, Johannes Kopf, Gordon Wetzstein, et al. 2024. Textured Gaussians for Enhanced 3D Scene Appearance Modeling. arXiv preprint arXiv:2411.18625 (2024).
- David Charatan, Sizhe Lester Li, Andrea Tagliasacchi, and Vincent Sitzmann. 2024. pixelsplat: 3d gaussian splats from image pairs for scalable generalizable 3d reconstruction. In Proceedings of the IEEE/CVF Conference on Computer Vision and Pattern Recognition. 19457-19467.
- Anpei Chen, Zexiang Xu, Andreas Geiger, Jingyi Yu, and Hao Su. 2022. TensoRF: Tensorial Radiance Fields. In Eur. Conf. Comput. Vis.
- Hanlin Chen, Chen Li, Yunsong Wang, and Gim Hee Lee. 2023. NeuSG: Neural Implicit Surface Reconstruction with 3D Gaussian Splatting Guidance. arXiv.org 2312.00846 (2023)
- Yuedong Chen, Haofei Xu, Chuanxia Zheng, Bohan Zhuang, Marc Pollefeys, Andreas Geiger, Tat-Jen Cham, and Jianfei Cai. 2024. Mvsplat: Efficient 3d gaussian splatting from sparse multi-view images. In European Conference on Computer Vision.
- Jaeyoung Chung, Jeongtaek Oh, and Kyoung Mu Lee. 2024. Depth-regularized optimization for 3d gaussian splatting in few-shot images. In Proceedings of the IEEE/CVF Conference on Computer Vision and Pattern Recognition. 811-820.
- Pinxuan Dai, Jiamin Xu, Wenxiang Xie, Xinguo Liu, Huamin Wang, and Weiwei Xu. 2024a. High-quality Surface Reconstruction using Gaussian Surfels. In Proc. of
- Pinxuan Dai, Jiamin Xu, Wenxiang Xie, Xinguo Liu, Huamin Wang, and Weiwei Xu. 2024b. High-quality Surface Reconstruction using Gaussian Surfels. In ACM SIG-GRAPH 2024 Conference Papers. Association for Computing Machinery, Article 22,
- Jinlong Fan, Xuepu Zeng, Jing Zhang, Mingming Gong, Yuxiang Yang, and Dacheng Tao. 2025. Advances in Radiance Field for Dynamic Scene: From Neural Field to Gaussian Field. arXiv preprint arXiv:2505.10049 (2025).
- Zhiwen Fan, Kevin Wang, Kairun Wen, Zehao Zhu, Dejia Xu, and Zhangyang Wang. 2023. LightGaussian: Unbounded 3D Gaussian Compression with 15x Reduction and 200+ FPS. arXiv:2311.17245 [cs.CV]
- John Flynn, Ivan Neulander, James Philbin, and Noah Snavely. 2016. Deepstereo: Learning to predict new views from the world's imagery. In Proceedings of the IEEE conference on computer vision and pattern recognition. 5515-5524.

- Guangcong, Zhaoxi Chen, Chen Change Loy, and Ziwei Liu. 2023. SparseNeRF: Distilling Depth Ranking for Few-shot Novel View Synthesis. IEEE/CVF International Conference on Computer Vision (ICCV) (2023).
- Antoine Guédon and Vincent Lepetit. 2024a. SuGaR: Surface-Aligned Gaussian Splatting for Efficient 3D Mesh Reconstruction and High-Quality Mesh Rendering. In IEEE Conf. Comput. Vis. Pattern Recog.
- Antoine Guédon and Vincent Lepetit. 2024b. Sugar: Surface-aligned gaussian splatting for efficient 3d mesh reconstruction and high-quality mesh rendering. In Proceedings of the IEEE/CVF Conference on Computer Vision and Pattern Recognition. 5354-5363.
- Binbin Huang, Zehao Yu, Anpei Chen, Andreas Geiger, and Shenghua Gao. 2024. 2D Gaussian Splatting for Geometrically Accurate Radiance Fields. In SIGGRAPH 2024 Conference Papers. Association for Computing Machinery. doi:10.1145/3641519.
- Zhentao Huang and Minglun Gong. 2024. Textured-GS: Gaussian Splatting with Spatially Defined Color and Opacity. arXiv preprint arXiv:2407.09733 (2024).
- Bernhard Kerbl, Georgios Kopanas, Thomas Leimkühler, and George Drettakis. 2023. 3d gaussian splatting for real-time radiance field rendering. ACM Trans. Graph. 42, 4 (2023), 139-1.
- Shakiba Kheradmand, Daniel Rebain, Gopal Sharma, Weiwei Sun, Yang-Che Tseng, Hossam Isack, Abhishek Kar, Andrea Tagliasacchi, and Kwang Moo Yi. 2024. 3d gaussian splatting as markov chain monte carlo. Advances in Neural Information Processing Systems 37 (2024), 80965-80986.
- Jiahui Lei, Yijia Weng, Adam Harley, Leonidas Guibas, and Kostas Daniilidis. 2024. Mosca: Dynamic gaussian fusion from casual videos via 4d motion scaffolds. arXiv preprint arXiv:2405.17421 (2024).
- Haolin Li, Jinyang Liu, Mario Sznaier, and Octavia Camps. 2025. 3d-hgs: 3d half-gaussian splatting. In IEEE Conf. Comput. Vis. Pattern Recog.
- Tianye Li, Mira Slavcheva, Michael Zollhoefer, Simon Green, Christoph Lassner, Changil Kim, Tanner Schmidt, Steven Lovegrove, Michael Goesele, Richard Newcombe, et al. 2022. Neural 3d video synthesis from multi-view video. In Proceedings of the IEEE/CVF Conference on Computer Vision and Pattern Recognition, 5521-5531.
- Zhaoshuo Li, Thomas Müller, Alex Evans, Russell H Taylor, Mathias Unberath, Ming-Yu Liu, and Chen-Hsuan Lin. 2023. Neuralangelo: High-Fidelity Neural Surface Reconstruction. In IEEE Conf. Comput. Vis. Pattern Recog.
- Tao Lu, Mulin Yu, Linning Xu, Yuanbo Xiangli, Limin Wang, Dahua Lin, and Bo Dai. 2024b. Scaffold-gs: Structured 3d gaussians for view-adaptive rendering. In Pro $ceedings\ of\ the\ IEEE/CVF\ Conference\ on\ Computer\ Vision\ and\ Pattern\ Recognition.$ 20654-20664.
- Zhicheng Lu, Xiang Guo, Le Hui, Tianrui Chen, Min Yang, Xiao Tang, Feng Zhu, and Yuchao Dai. 2024a. 3d geometry-aware deformable gaussian splatting for dynamic view synthesis. In Proceedings of the IEEE/CVF Conference on Computer Vision and Pattern Recognition. 8900-8910.
- Marko Mihajlovic, Sergey Prokudin, Marc Pollefeys, and Siyu Tang. 2024a. ResFields: Residual Neural Fields for Spatiotemporal Signals. In International Conference on Learning Representations (ICLR).
- Marko Mihajlovic, Sergey Prokudin, Siyu Tang, Robert Maier, Federica Bogo, Tony Tung, and Edmond Boyer. 2024b. SplatFields: Neural Gaussian Splats for Sparse 3D and 4D Reconstruction. In European Conference on Computer Vision (ECCV). Springer.
- Ben Mildenhall, Pratul P Srinivasan, Matthew Tancik, Jonathan T Barron, Ravi Ramamoorthi, and Ren Ng. 2020. Nerf: Representing scenes as neural radiance fields for view synthesis. In Eur. Conf. Comput. Vis.
- Thomas Müller, Alex Evans, Christoph Schied, and Alexander Keller. 2022. Instant neural graphics primitives with a multiresolution hash encoding. ACM transactions on graphics (TOG) 41, 4 (2022), 1-15.
- Michael Oechsle, Songyou Peng, and Andreas Geiger. 2021. UNISURF: Unifying Neural Implicit Surfaces and Radiance Fields for Multi-View Reconstruction. In Int. Conf.
- Keunhong Park, Utkarsh Sinha, Jonathan T Barron, Sofien Bouaziz, Dan B Goldman, Steven M Seitz, and Ricardo Martin-Brualla. 2021a. Nerfies: Deformable neural radiance fields. In Proceedings of the IEEE/CVF international conference on computer vision. 5865-5874.
- Keunhong Park, Utkarsh Sinha, Peter Hedman, Jonathan T. Barron, Sofien Bouaziz, Dan B Goldman, Ricardo Martin-Brualla, and Steven M. Seitz. 2021b. HyperNeRF: A Higher-Dimensional Representation for Topologically Varying Neural Radiance Fields. ACM Trans. Graph. 40, 6, Article 238 (dec 2021).
- Songyou Peng, Michael Niemeyer, Lars Mescheder, Marc Pollefeys, and Andreas Geiger. 2020. Convolutional Occupancy Networks. In Eur. Conf. Comput. Vis.
- Albert Pumarola, Enric Corona, Gerard Pons-Moll, and Francesc Moreno-Noguer. 2021. D-nerf: Neural radiance fields for dynamic scenes. In Proceedings of the IEEE/CVF conference on computer vision and pattern recognition. 10318-10327
- Zhiyin Qian, Shaofei Wang, Marko Mihajlovic, Andreas Geiger, and Siyu Tang. 2024. 3dgs-avatar: Animatable avatars via deformable 3d gaussian splatting. In Proceedings of the IEEE/CVF conference on computer vision and pattern recognition. 5020-5030.
- Christian Reiser, Stephan Garbin, Pratul Srinivasan, Dor Verbin, Richard Szeliski, Ben Mildenhall, Jonathan Barron, Peter Hedman, and Andreas Geiger. 2024. Binary

- opacity grids: Capturing fine geometric detail for mesh-based view synthesis. ACM Transactions on Graphics (TOG) 43, 4 (2024), 1–14.
- Christian Reiser, Songyou Peng, Yiyi Liao, and Andreas Geiger. 2021. Kilonerf: Speeding up neural radiance fields with thousands of tiny mlps. In Proceedings of the IEEE/CVF international conference on computer vision. 14335–14345.
- Victor Rong, Jingxiang Chen, Sherwin Bahmani, Kiriakos N Kutulakos, and David B Lindell. 2024. Gstex: Per-primitive texturing of 2d gaussian splatting for decoupled appearance and geometry modeling. arXiv preprint arXiv:2409.12954 (2024).
- Radu Alexandru Rosu and Sven Behnke. 2023. PermutoSDF: Fast Multi-View Reconstruction with Implicit Surfaces using Permutohedral Lattices. In IEEE Conf. Comput. Vis. Pattern Recog.
- Ruoxi Shi, Xinyue Wei, Cheng Wang, and Hao Su. 2024. ZeroRF: Fast Sparse View 360deg Reconstruction with Zero Pretraining. In IEEE Conf. Comput. Vis. Pattern Recog.
- Vincent Sitzmann, Julien N.P. Martel, Alexander W. Bergman, David B. Lindell, and Gordon Wetzstein. 2020. Implicit Neural Representations with Periodic Activation Functions. In Advances in Neural Information Processing Systems (NeurIPS).
- Vincent Sitzmann, Michael Zollhöfer, and Gordon Wetzstein. 2019. Scene representation networks: Continuous 3d-structure-aware neural scene representations. In Advances in Neural Information Processing Systems (NeurIPS).
- Yunzhou Song, Heguang Lin, Jiahui Lei, Lingjie Liu, and Kostas Daniilidis. 2024. HDGS: Textured 2D Gaussian Splatting for Enhanced Scene Rendering. arXiv:2412.01823 [cs.CV] https://arxiv.org/abs/2412.01823
- Cheng Sun, Min Sun, and Hwann-Tzong Chen. 2022. Direct voxel grid optimization: Super-fast convergence for radiance fields reconstruction. In *Proceedings of the IEEE/CVF conference on computer vision and pattern recognition*. 5459–5469.
- Jiakai Sun, Han Jiao, Guangyuan Li, Zhanjie Zhang, Lei Zhao, and Wei Xing. 2024. 3dgstream: On-the-fly training of 3d gaussians for efficient streaming of photorealistic free-viewpoint videos. In Proceedings of the IEEE/CVF Conference on Computer Vision and Pattern Recognition. 20675–20685.
- David Svitov, Pietro Morerio, Lourdes Agapito, and Alessio Del Bue. 2024. BillBoard Splatting (BBSplat): Learnable Textured Primitives for Novel View Synthesis. arXiv preprint arXiv:2411.08508 (2024).
- Zhenggang Tang, Yuchen Fan, Dilin Wang, Hongyu Xu, Rakesh Ranjan, Alexander Schwing, and Zhicheng Yan. 2024. MV-DUSt3R+: Single-Stage Scene Reconstruction from Sparse Views In 2 Seconds. arXiv preprint arXiv:2412.06974 (2024).
- Ayush Tewari, Justus Thies, Ben Mildenhall, Pratul Srinivasan, Edgar Tretschk, Wang Yifan, Christoph Lassner, Vincent Sitzmann, Ricardo Martin-Brualla, Stephen Lombardi, et al. 2022. Advances in neural rendering. In *Computer Graphics Forum*.
- Matias Turkulainen, Xuqian Ren, Iaroslav Melekhov, Otto Seiskari, Esa Rahtu, and Juho Kannala. 2024. DN-Splatter: Depth and Normal Priors for Gaussian Splatting and Meshing. In IEEE Winter Conference on Applications of Computer Vision (WACV).
- Peng Wang, Lingjie Liu, Yuan Liu, Christian Theobalt, Taku Komura, and Wenping Wang. 2021. NeuS: Learning Neural Implicit Surfaces by Volume Rendering for Multi-view Reconstruction. In Advances in Neural Information Processing Systems (NeurIPS).
- Yiming Wang, Qin Han, Marc Habermann, Kostas Daniilidis, Christian Theobalt, and Lingjie Liu. 2023. NeuS2: Fast Learning of Neural Implicit Surfaces for Multi-view Reconstruction. In Int. Conf. Comput. Vis.
- Zhou Wang, Alan C Bovik, Hamid R Sheikh, and Eero P Simoncelli. 2004. Image quality assessment: from error visibility to structural similarity. *IEEE transactions on image* processing 13, 4 (2004), 600–612.
- Guanjun Wu, Taoran Yi, Jiemin Fang, Lingxi Xie, Xiaopeng Zhang, Wei Wei, Wenyu Liu, Qi Tian, and Xinggang Wang. 2024a. 4D Gaussian Splatting for Real-Time Dynamic Scene Rendering. In IEEE Conf. Comput. Vis. Pattern Recog.
- Guanjun Wu, Taoran Yi, Jiemin Fang, Lingxi Xie, Xiaopeng Zhang, Wei Wei, Wenyu Liu, Qi Tian, and Xinggang Wang. 2024b. 4d gaussian splatting for real-time dynamic scene rendering. In Proceedings of the IEEE/CVF conference on computer vision and pattern recognition. 20310–20320.
- Guanjun Wu, Taoran Yi, Jiemin Fang, Lingxi Xie, Xiaopeng Zhang, Wei Wei, Wenyu Liu, Qi Tian, and Xinggang Wang. 2024c. 4D Gaussian Splatting for Real-Time Dynamic Scene Rendering. In Proceedings of the IEEE/CVF Conference on Computer Vision and Pattern Recognition (CVPR). 20310–20320.
- Rui Xu, Wenyue Chen, Jiepeng Wang, Yuan Liu, Peng Wang, Lin Gao, Shiqing Xin, Taku Komura, Xin Li, and Wenping Wang. 2024a. SuperGaussians: Enhancing Gaussian Splatting Using Primitives with Spatially Varying Colors. arXiv preprint arXiv:2411.18966 (2024).
- Tian-Xing Xu, Wenbo Hu, Yu-Kun Lai, Ying Shan, and Song-Hai Zhang. 2024b. Texture-gs: Disentangling the geometry and texture for 3d gaussian splatting editing. In European Conference on Computer Vision. Springer, 37–53.
- Yi Xu, Yao Lu, and Ziyu Wen. 2017. Owlii Dynamic human mesh sequence dataset. In ISO/IEC JTC1/SC29/WG11 m41658, 120th MPEG Meeting.
- Ziyi Yang, Xinyu Gao, Wen Zhou, Shaohui Jiao, Yuqing Zhang, and Xiaogang Jin. 2023. Deformable 3D Gaussians for High-Fidelity Monocular Dynamic Scene Reconstruction. arXiv preprint arXiv:2309.13101 (2023).

- Ziyi Yang, Xinyu Gao, Wen Zhou, Shaohui Jiao, Yuqing Zhang, and Xiaogang Jin. 2024a. Deformable 3d gaussians for high-fidelity monocular dynamic scene reconstruction. In Proceedings of the IEEE/CVF conference on computer vision and pattern recognition. 2031–20341.
- Zeyu Yang, Hongye Yang, Zijie Pan, and Li Zhang. 2024b. Real-time Photorealistic Dynamic Scene Representation and Rendering with 4D Gaussian Splatting. In *International Conference on Learning Representations (ICLR)*.
- Lior Yariv, Jiatao Gu, Yoni Kasten, and Yaron Lipman. 2021. Volume rendering of neural implicit surfaces. In Advances in Neural Information Processing Systems (NeurIPS).
- Lior Yariv, Peter Hedman, Christian Reiser, Dor Verbin, Pratul P. Srinivasan, Richard Szeliski, Jonathan T. Barron, and Ben Mildenhall. 2023. BakedSDF: Meshing Neural SDFs for Real-Time View Synthesis. In Proc. of SIGGRAPH.
- Heng Yu, Joel Julin, Zoltán Á Milacski, Koichiro Niinuma, and László A Jeni. 2024b. Cogs: Controllable gaussian splatting. In Proceedings of the IEEE/CVF Conference on Computer Vision and Pattern Recognition.
- Mulin Yu, Tao Lu, Linning Xu, Lihan Jiang, Yuanbo Xiangli, and Bo Dai. 2024c. GSDF: 3DGS Meets SDF for Improved Rendering and Reconstruction. In Advances in Neural Information Processing Systems (NeurIPS).
- Zehao Yu, Anpei Chen, Binbin Huang, Torsten Sattler, and Andreas Geiger. 2024a. Mip-Splatting: Alias-free 3D Gaussian Splatting. Conference on Computer Vision and Pattern Recognition (CVPR) (2024).
- Zehao Yu, Torsten Sattler, and Andreas Geiger. 2024d. Gaussian Opacity Fields: Efficient Adaptive Surface Reconstruction in Unbounded Scenes. ACM Transactions on Graphics (2024).
- Zehao Yu, Torsten Sattler, and Andreas Geiger. 2024e. Gaussian Opacity Fields: Efficient Adaptive Surface Reconstruction in Unbounded Scenes. ACM Trans. Graph. 43, 6 (2024), 271:1–271:13.
- Chuanrui Zhang, Yingshuang Zou, Zhuoling Li, Minmin Yi, and Haoqian Wang. 2025b. Transplat: Generalizable 3d gaussian splatting from sparse multi-view images with transformers. In Proceedings of the AAAI Conference on Artificial Intelligence.
- Richard Zhang, Phillip Isola, Alexei A Efros, Eli Shechtman, and Oliver Wang. 2018. The unreasonable effectiveness of deep features as a perceptual metric. In Proceedings of the IEEE conference on computer vision and pattern recognition. 586–595.
- Xin Zhang, Anpei Chen, Jincheng Xiong, Pinxuan Dai, Yujun Shen, and Weiwei Xu. 2025a. Neural Shell Texture Splatting: More Details and Fewer Primitives. In Proceedings of the IEEE/CVF International Conference on Computer Vision (ICCV).
- Tinghui Zhou, Richard Tucker, John Flynn, Graham Fyffe, and Noah Snavely. 2018. Stereo Magnification: Learning View Synthesis using Multiplane Images. In SIG-GRAPH.
- Jialin Zhu, Jiangbei Yue, Feixiang He, and He Wang. 2025. 3D Student Splatting and Scooping. In IEEE Conf. Comput. Vis. Pattern Recog.
- Ruijie Zhu, Yanzhe Liang, Hanzhi Chang, Jiacheng Deng, Jiahao Lu, Wenfei Yang, Tianzhu Zhang, and Yongdong Zhang. 2024. Motiongs: Exploring explicit motion guidance for deformable 3d gaussian splatting. In Advances in Neural Information Processing Systems (NeurIPS).
- Matthias Zwicker, Hanspeter Pfister, Jeroen Van Baar, and Markus Gross. 2002. EWA splatting. IEEE Transactions on Visualization and Computer Graphics 8, 3 (2002), 223–238



96 95 WS 93 PSNR 5 92 91 90

Fig. 4. Average PSNR and SSIM curves with varying input views on Blender under the sparse-view setup. Our method consistently improves upon Splat Fields across input views ranging from 4 to 10.

Fig. 5. Average PSNR and SSIM curves with varying input views on Owlii under the sparse-view dynamic setup. Our method consistently improves upon SplatFields across input views ranging from 4 to 10.

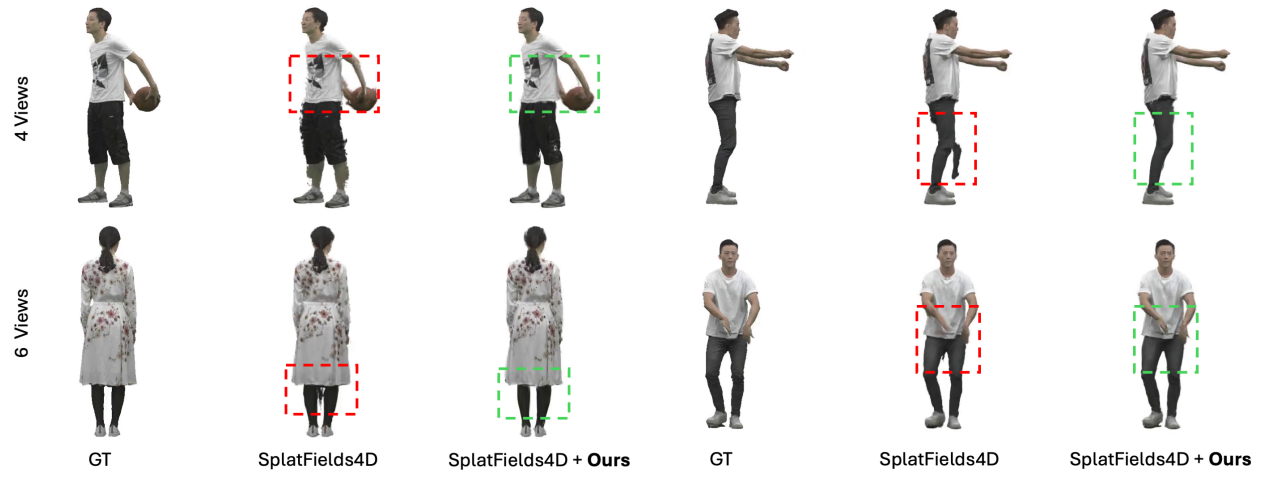


Fig. 6. Qualitative results for sparse-view dynamic reconstruction on Owlii using 4 and 6 input views. Our method effectively reduces floaters and inaccurate boundaries compared to SplatFields.



Fig. 7. Qualitative results for sparse-view dynamic reconstruction on Owlii using 10 input views. Our method can capture finer details compared to SplatFields.

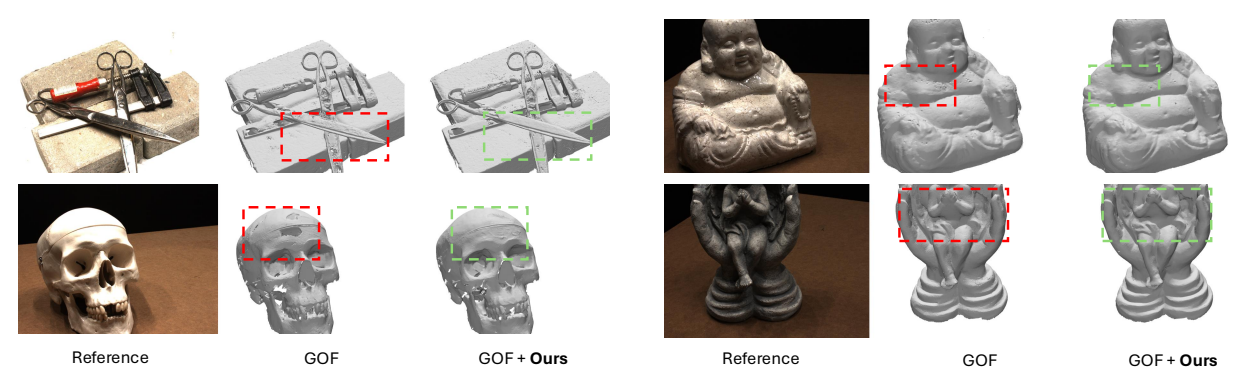


Fig. 8. Qualitative comparison of surface reconstruction results on the DTU dataset. Our method improves the mesh quality for both surface extraction approaches used in GOF: TSDF Fusion (first row) and GOF's proposed method (second row).

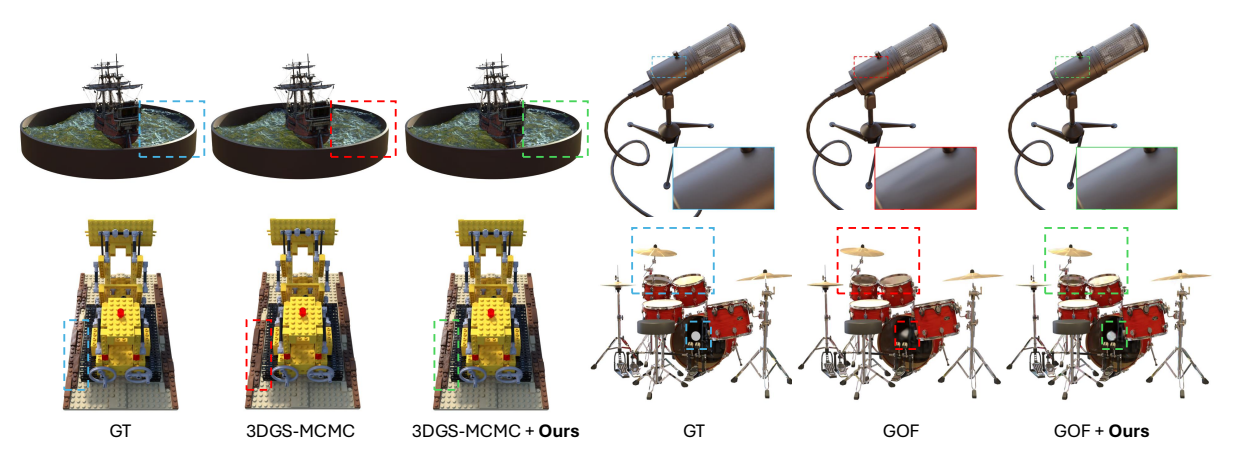


Fig. 9. **Qualitative Comparison on Blender using 100 input views.** The proposed neural texture representation produces smoother geometry while capturing high-frequency appearance details.

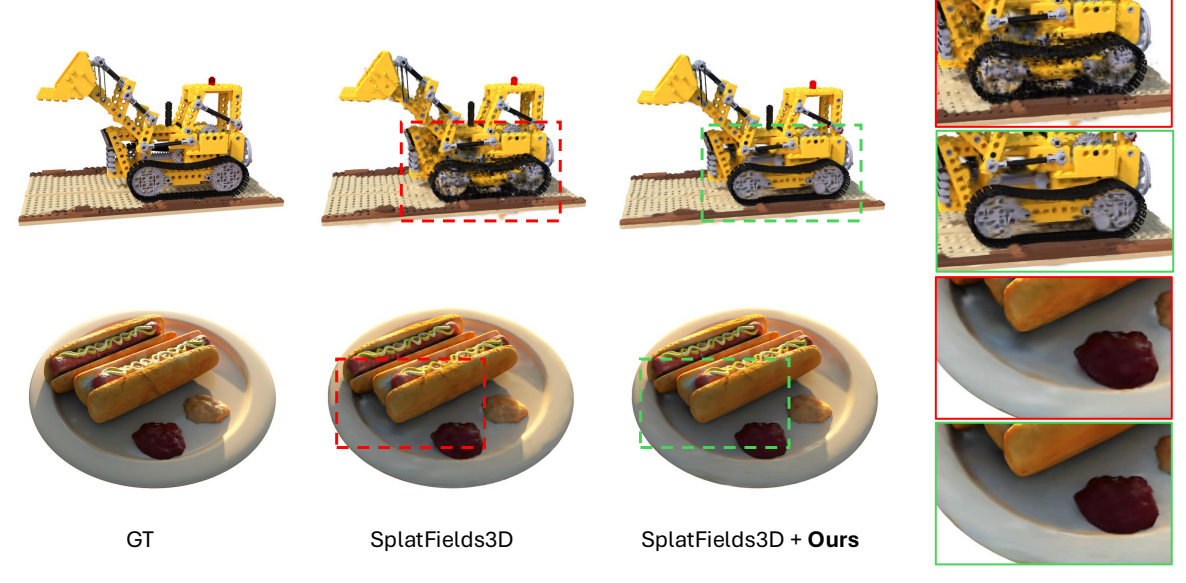


Fig. 10. **Qualitative results for sparse-view reconstruction on Blender using 10 input views.** Our method yields sharper reconstructions with more accurate geometry.

Neural Texture Splatting: Expressive 3D Gaussian Splatting for View Synthesis, Geometry, and Dynamic Reconstruction -Supplementary

Yiming Wang, Shaofei Wang, Marko Mihajlovic, Siyu Tang ETH Zurich, Switzerland

Appendix

A Implementation details

Model Parameters

We use a tri-plane of size $192 \times 192 \times 16$ across all scenes for the global neural field. The associated neural network has a width of 128, consists of two hidden layers. To enhance representational capacity in dense-view reconstruction tasks, we use separate learnable global tri-planes and distinct neural network architectures for modeling RGB textures and alpha textures. We adopt a standard linear MLP with ReLU activation for color decoding, while a SIREN network [Sitzmann et al. 2020] is adopted for alpha decoding. For sparse-view reconstruction of static and dynamic scenes, we build upon SplatFields by employing a CNN-based tri-plane generator [Shi et al. 2024] to provide a deep structural prior, and utilize the Res-Fields MLP [Mihajlovic et al. 2024a] for decoding of color and alpha values. For our local tri-plane texture resolution τ , we set $\tau = 8$ when evaluating on the Blender dataset [Mildenhall et al. 2020] and DTU dataset [Aanæs et al. 2016], and $\tau = 4$ for all other experiments.

A.2 Training Details

We run all experiments on NVIDIA RTX 4090 GPUs, except for running Mip-NeRF360 on NVIDIA H200 due to additional memory

Sparse-view Scene Reconstruction. We adopt the training setup and hyperparameter configurations from SplatFields to ensure a fair and consistent comparison across all experiments. For the Blender dataset, both SplatFields and our method are trained for 40k iterations using identical configurations. Our model is initialized from the SplatFields checkpoint at 20k iterations and jointly trained for the remaining 20k iterations. For dynamic scene reconstruction on the Owlii dataset, both SplatFields and our method are trained for 200k iterations. Specifically, our model is initialized from the SplatFields checkpoint at 100k iterations and trained jointly for an additional 100k iterations.

Dense-view Scene Reconstruction. Following the standard training protocol commonly adopted in 3DGS-based methods, we train all models for 30k iterations on the Blender and Mip-NeRF360 datasets. In our setup, we first pretrain the backbone network for 5k iterations, followed by 25k iterations of joint training with our proposed module. All experiments use the same hyperparameters and optimization settings to ensure a fair comparison.

Table 10. Comparison of 2D Texture and 3D Texture modelling on Blender. Modeling our RGBA Texture Field with either 2D or 3D textures leads to improvements over the baseline.

Method	PSNR↑	SSIM↑	LPIPS↓
GoF	33.44	0.9698	0.0307
+ Ours (2D Texture) + Ours (3D Texture)	33.93 34.09	0.9705 0.9710	0.0290 0.0286

Table 11. Efficiency analysis on GOF. We report the average training time and rendering speed on the Blender dataset using the original GOF* implementation as released in the paper. Note that the latest version of GOF* merges CUDA operations, achieving a 2× speed-up, an optimization also applicable to our method. While our proposed module introduces additional computational overhead compared to GOF*, this trade-off yields significantly improved performance in both novel view synthesis metrics on Blender and surface reconstruction accuracy (CD) on DTU.

Method	CD↓	PSNR↑	SSIM↑	LPIPS↓	Training (min)	FPS
GOF*	0.74	33.44	0.9698	0.0307	39.50	28.32
GOF* + Ours	0.67	34.09	0.9710	0.0286	61.78	20.82

Table 12. Comparison with State-of-the-art per-primitive texture methods Textured-GS on Blender and Mip-NeRF360. We report the disk storage required for storing textures. Our NTS achieves higher PSNR while using less storage.

Method	PSNR↑	Blender Model Size (MB)	MipNeRF360) PSNR↑ Model Size (MB)		
Textured Gaussians	33.24	~51M	27.35	~854M	
GOF + Ours	34.09	~15M	27.69	~15M	
3DGS-MCMC + Ours	34.06	~15M	28.24	~15M	

Supplementary Ablation Results

Modeling the RGBA Texture Field. We explore a simplified approximation of the RGBA volume using a single 2D plane, aligned with the splat's principal axis. As shown in Tab. 10, when combined with our Neural Texture method, both representations improve upon the baseline. We adopt the 3D tri-plane representation for modeling the RGBA texture field throughout this paper.

Efficiency Analysis. An efficiency analysis of our method is presented in Table 11, with experiments conducted on an NVIDIA RTX 4090 GPU. While our approach significantly improves upon the baseline performance, it comes with increased computational cost during training and a slight decrease in rendering speed. A more detailed discussion is provided in the Limitations section.

Table 13. Quantitative Comparison on Sparse-View Dynamic Scene Reconstruction (10 Input Views). SSIM values are scaled by a factor of 100 for readability; coloring 1st, 2nd, and 3rd highlight best results.

Method				PSNR ↑		
		Mean	Dancer	Exercise	Model	Basketball
10	DyNeRF	29.70	28.22	30.64	29.95	30.00
Z.	TNeRF	30.39	29.12	31.00	30.71	30.71
Š	DNeRF	30.25	29.39	30.63	30.63	30.35
4D NeRFs	Nerfies	30.70	29.57	31.08	30.53	31.60
4	HyperNeRF	30.36	30.09	30.39	30.88	30.08
	4D-GS	28.05	28.11	29.09	29.06	25.94
ing.	Deformable3DGS	27.76	27.86	28.78	26.47	27.95
Splatting	4DGaussians	29.80	28.46	30.21	30.69	29.82
	SplatFields4D	31.32	31.05	31.16	31.50	31.58
	SplatFields4D + Ours	32.09	31.79	31.84	32.41	32.30
				SSIM ↑		
		Mean	Dancer	Exercise	Model	Basketball
	4D-GS	95.34	95.31	95.96	94.92	95.16
	Deformable3DGS	93.80	94.10	95.09	91.58	94.43
	4DGaussians	95.91	95.19	96.47	95.71	96.28
	SplatFields4D	96.81	96.76	96.92	96.32	97.23
	SplatFields4D + Ours	97.34	97.31	97.31	97.10	97.65
				LPIPS ↓		
		Mean	Dancer	Exercise	Model	Basketball
	SplatFields4D	6.01	5.90	6.62	6.30	5.21
	SplatFields4D + Ours	5.45	5.20	6.20	5.60	4.79

Table 14. Quantitative Comparison on Sparse-View Dynamic Scene Reconstruction (8 Input Views). SSIM values are scaled by a factor of 100 for readability; coloring 1st, 2nd, and 3rd highlight best results.

			PSNR ↑		
Method	Mean	Dancer	Exercise	Model	Basketball
4D-GS	26.20	26.99	26.34	27.41	24.07
Deformable3DGS	26.06	26.77	26.24	25.61	25.62
4DGaussians	28.16	27.34	28.10	29.60	27.62
SplatFields4D	29.84	29.92	29.16	30.10	30.18
SplatFields4D + Ours	30.67	30.61	30.16	31.19	30.70
			SSIM ↑		
	Mean	Dancer	Exercise	Model	Basketball
4D-GS	93.71	94.19	93.94	93.29	93.40
Deformable3DGS	92.37	93.24	93.29	90.33	92.62
4DGaussians	95.00	94.39	95.45	94.92	95.26
SplatFields4D	96.28	96.31	96.26	95.78	96.77
SplatFields4D + Ours	96.75	96.85	96.65	96.56	96.94
			LPIPS J		
	Mean	Dancer	Exercise	Model	Basketball
SplatFields4D	6.26	6.14	6.93	6.53	5.44
SplatFields4D + Ours	6.06	5.70	6.82	6.12	5.60

Comparison with TexturedGaussians. We further demonstrate the advantages of our neural texture modeling by comparing it to a concurrent method, Textured Gaussians [Chao et al. 2024], which employs per-primitive 2D RGBA textures to enhance 3DGS performance. We report its performance metrics as stated in the original paper and estimate its model size based on the reported number of primitives and texture resolution. As shown in Table 12, our method

Table 15. Quantitative Comparison on Sparse-View Dynamic Scene Reconstruction (6 Input Views). SSIM values are scaled by a factor of 100 for readability; coloring 1st, 2nd, and 3rd highlight best results.

Method			PSNR ↑			
Metnod	Mean	Dancer	Exercise	Model	Basketball	
4D-GS	21.42	22.89	20.80	21.60	20.40	
Deformable3DGS	24.46	25.37	24.31	24.12	24.02	
4DGaussians	26.52	26.13	26.27	27.34	26.36	
SplatFields4D	28.36	28.84	27.54	28.67	28.39	
SplatFields4D + Ours	29.19	29.58	28.42	29.59	29.19	
			SSIM ↑			
	Mean	Dancer	Exercise	Model	Basketball	
4D-GS	87.23	89.52	87.05	85.16	87.20	
Deformable3DGS	90.95	91.73	91.48	89.11	91.48	
4DGaussians	93.87	93.58	94.45	93.05	94.40	
SplatFields4D	95.69	95.99	95.71	94.85	96.21	
SplatFields4D + Ours	96.16	96.47	96.05	95.62	96.49	
			LPIPS ↓			
	Mean	Dancer	Exercise	Model	Basketball	
SplatFields4D	6.60	6.26	7.16	7.27	5.73	
SplatFields4D + Ours	6.36	5.88	7.08	6.75	5.72	

Table 16. Quantitative Comparison on Sparse-View Dynamic Scene Reconstruction (4 Input Views). SSIM and LPIPS values are scaled by a factor of 100 for readability; coloring 1st, 2nd, and 3rd highlight best results.

Method	Mean	Dancer	PSNR ↑ Exercise	Model	Basketball		
4D-GS	17.40	17.70	16.86	18.35	16.71		
Deformable3DGS	20.04	21.42	19.56	19.71	19.45		
4DGaussians	21.31	21.49	21.05	21.90	20.80		
SplatFields4D	21.95	22.83	20.76	21.83	22.39		
SplatFields4D + Ours	25.05	26.19	24.54	23.65	25.81		
			SSIM ↑				
	Mean	Dancer	Exercise	Model	Basketball		
4D-GS	78.94	80.81	78.72	78.09	78.15		
Deformable3DGS	87.10	89.04	87.67	85.05	86.63		
4DGaussians	89.50	90.34	90.67	87.47	89.51		
SplatFields4D	91.60	92.89	92.07	89.02	92.41		
SplatFields4D + Ours	93.19	94.50	93.62	90.61	94.02		
			LPIPS ↓				
	Mean	Dancer	Exercise	Model	Basketball		
SplatFields4D	9.86	8.82	10.23	11.27	9.14		
SplatFields4D + Ours	8.91	7.63	9.60	10.23	8.20		

achieves significantly higher performance while requiring a much smaller model size, resulting in substantial reductions in storage overhead.

C Additional Quantitative Results

We provided complete benchmarking for sparse-view reconstruction of the static scene on the Blender and Owlii datasets.

Table 18. Quantitative Comparison on Sparse-View Novel View Synthesis in Blender (8 Input Views). SSIM values are scaled by a factor of 100 for readability; coloring 1st , 2nd , and 3rd highlight best results.

-											
Method		_			PSNR	•					
	mean	Toy	Ficus	Hotdog	Chair	Mic	Ship	Drums	Materials		
SparseNeRF	-	22.33	17.97	-	23.81	23.01	19.85	17.85	20.02		
SparseNeRF wo. depth	22.20	24.06	18.42	27.09	25.12	23.04	21.23	17.94	20.74		
SuGaR	20.62	21.91	22.33	23.01	23.30	18.60	19.59	18.66	17.55		
ScaffoldGS	21.53	20.95	21.35	23.77	22.77	26.40	18.88	18.96	19.17		
Mip-Splatting	22.37	22.05	23.23	24.24	23.57	26.32	19.91	20.10	19.55		
3DGS	22.93	22.55	23.69	25.57	24.43	27.37	19.98	20.33	19.49		
LightGaussian	22.98	22.67	24.98	24.79	24.40	26.59	20.60	20.41	19.41		
2DGS	23.04	22.19	23.63	26.76	25.46	26.24	20.16	20.60	19.25		
SplatFields3D	23.98	24.71	23.97	27.87	25.64	26.49	22.15	21.12	19.85		
SplatFields3D + Ours	24.09	25.40	23.16	27.97	25.30	26.54	22.40	21.24	20.67		
	SSIM ↑										
	mean	Toy	Ficus	Hotdog	Chair	Mic	Ship	Drums	Materials		
SparseNeRF	-	84.85	83.98	-	88.39	92.06	74.32	81.44	83.66		
SparseNeRF wo. depth	86.30	88.27	83.97	93.65	90.23	92.15	76.01	81.38	84.78		
SuGaR	82.74	82.04	87.95	89.41	87.60	85.08	72.80	79.84	77.23		
ScaffoldGS	83.62	80.54	88.25	89.04	86.23	95.01	68.49	81.49	79.91		
Mip-Splatting	86.24	82.93	91.03	90.84	89.21	95.77	71.86	86.15	82.14		
3DGS	86.63	84.05	91.56	91.63	90.49	95.99	70.96	86.62	81.76		
LightGaussian	87.11	84.44	93.01	91.47	90.17	95.76	72.16	86.97	82.92		
2DGS	87.72	84.80	91.74	93.13	91.79	95.72	74.06	87.89	82.65		
SplatFields3D	88.94	88.04	91.69	94.68	90.91	95.48	78.76	88.50	83.46		
SplatFields3D + Ours	89.14	88.71	91.01	94.77	90.38	95.27	78.79	88.73	85.47		
					LPIPS	1					
	mean	Toy	Ficus	Hotdog	Chair	Mic	Ship	Drums	Materials		
SplatFields3D	11.92	12.14	7.93	8.29	10.08	4.52	25.91	10.28	16.21		
SplatFields3D + Ours	12.70	12.02	9.29	8.45	11.07	5.23	27.96	10.83	16.78		

Table 19. Quantitative Comparison on Sparse-View Novel View Synthesis in Blender (6 Input Views). SSIM values are scaled by a factor of 100 for readability; coloring 1st , 2nd , and 3rd highlight best results.

Method					PSNR '	↑				
Method	mean	Toy	Ficus	Hotdog	Chair	Mic	Ship	Drums	Materials	
SparseNeRF	-	20.86	18.03	-	22.75	22.40	19.33	16.24	19.54	
SparseNeRF wo. depth	20.86	22.62	17.63	25.84	22.65	20.72	19.85	17.25	20.30	
SuGaR	19.07	19.89	20.61	20.80	21.92	18.26	17.72	16.86	16.53	
ScaffoldGS	19.65	18.21	20.72	19.48	22.20	24.31	16.47	17.21	18.62	
Mip-Splatting	20.04	19.39	21.81	19.70	21.72	24.44	17.02	17.72	18.52	
3DGS	20.62	19.80	22.25	21.16	22.75	25.21	17.58	17.77	18.48	
LightGaussian	20.76	20.25	23.12	20.66	22.69	24.89	17.83	18.02	18.63	
2DGS	20.74	19.38	21.93	23.85	23.26	24.48	16.92	17.91	18.17	
SplatFields3D	22.26	22.41	22.26	26.19	25.03	24.84	19.33	18.97	19.05	
SplatFields3D + Ours	22.72	23.50	22.45	26.94	24.31	25.05	21.19	19.19	19.12	
	SSIM ↑									
	mean	Toy	Ficus	Hotdog	Chair	Mic	Ship	Drums	Materials	
SparseNeRF	-	83.25	83.70	-	87.76	91.53	72.96	78.58	83.47	
SparseNeRF wo. depth	84.42	85.68	82.33	92.51	87.47	90.72	72.50	79.58	84.59	
SuGaR	79.85	77.67	85.51	86.44	84.98	84.24	68.93	76.35	74.68	
ScaffoldGS	80.34	74.13	87.01	82.79	84.99	93.10	62.49	78.61	79.59	
Mip-Splatting	83.09	77.68	89.34	86.81	86.46	94.58	66.45	82.08	81.34	
3DGS	83.56	78.58	89.79	87.81	87.35	94.81	66.71	82.45	80.94	
LightGaussian	84.34	79.64	91.08	88.67	87.49	94.76	67.63	83.09	82.33	
2DGS	84.43	78.54	89.71	90.36	88.16	94.59	68.63	83.87	81.61	
SplatFields3D	86.62	84.05	89.56	93.62	89.53	94.50	74.14	85.03	82.55	
SplatFields3D + Ours	87.40	86.22	89.95	94.00	89.23	94.49	77.27	85.52	82.53	
					LPIPS	↓				
	mean	Toy	Ficus	Hotdog	Chair	Mic	Ship	Drums	Materials	
SplatFields3D	13.50	14.46	9.47	9.64	10.53	5.48	28.32	13.36	16.76	
SplatFields3D + Ours	13.32	13.87	8.86	9.72	11.02	5.44	27.64	13.05	16.95	

Table 20. Quantitative Comparison on Sparse-View Novel View Synthesis in Blender (4 Input Views). SSIM and LPIPS values are scaled by a factor of 100 for readability; coloring 1st , 2nd , and 3rd highlight best

Method					PSNR	1			
Wethou	mean	Toy	Ficus	Hotdog	Chair	Mic	Ship	Drums	Materials
SparseNeRF	-	20.94	17.48	23.81	21.41	21.52	-	15.37	17.03
SparseNeRF wo. depth	17.87	19.31	17.05	23.54	20.26	11.56	17.86	13.64	19.77
SuGaR	16.94	16.96	19.30	19.36	19.07	17.47	15.22	14.73	13.38
ScaffoldGS	16.86	15.40	19.58	17.31	18.40	20.54	14.70	15.27	13.69
Mip-Splatting	16.94	16.23	19.60	16.98	18.38	20.56	14.64	14.92	14.21
3DGS	17.37	16.44	19.72	18.65	18.72	20.75	15.43	15.08	14.15
LightGaussian	17.70	16.94	20.35	18.56	18.96	21.53	15.67	15.44	14.19
2DGS	17.58	16.32	19.69	20.67	19.39	21.17	14.45	14.84	14.14
SplatFields3D	19.16	18.89	20.19	24.31	19.31	21.73	16.83	16.35	15.69
SplatFields3D + Ours	19.98	18.94	20.39	23.79	20.26	23.75	17.34	17.38	17.97
					SSIM	Î.			
	mean	Toy	Ficus	Hotdog	Chair	Mic	Ship	Drums	Materials
SparseNeRF	-	83.38	82.98	90.95	85.14	90.49	-	76.46	79.48
SparseNeRF wo. depth	78.66	78.80	80.86	90.57	82.26	72.23	69.29	71.97	83.28
SuGaR	75.61	72.07	83.08	83.68	80.66	82.48	63.46	70.73	68.69
ScaffoldGS	74.99	68.04	84.68	76.92	77.58	90.24	59.60	71.20	71.68
Mip-Splatting	77.67	71.47	85.73	82.68	81.00	91.42	61.17	74.27	73.62
3DGS	78.12	72.17	85.97	83.78	81.49	91.55	62.05	74.80	73.18
LightGaussian	79.38	73.58	86.93	85.98	81.91	92.25	63.27	75.88	75.22
2DGS	79.26	72.84	86.04	86.62	82.54	92.04	63.57	76.25	74.14
SplatFields3D	82.26	78.23	86.17	92.10	83.85	91.92	70.40	78.67	76.77
SplatFields3D + Ours	83.51	77.33	87.48	91.92	85.24	93.46	71.51	80.33	80.85
					LPIPS	1			
	mean	Toy	Ficus	Hotdog	Chair	Mic	Ship	Drums	Materials
SplatFields3D	17.56	19.56	12.20	11.41	16.16	8.35	31.97	19.06	21.76
SplatFields3D + Ours	16.93	20.49	9.34	12.10	15.81	6.89	32.72	17.82	20.28

Table 17. Quantitative Comparison on Sparse-View Novel View Synthesis in Blender (10 Input Views). SSIM values are scaled by a factor of 100 for readability; coloring 1st, 2nd, and 3rd highlight best results.

M-41-J					PSNR '	1			
Method	mean	Toy	Ficus	Hotdog	Chair	Mic	Ship	Drums	Materials
SparseNeRF	-	22.64	18.27	-	25.30	23.27	20.29	18.61	19.72
SparseNeRF wo. depth	22.58	23.89	18.75	27.56	26.42	23.23	21.68	18.20	20.87
SuGaR	21.10	22.78	22.42	23.60	24.25	17.93	20.35	19.11	18.40
ScaffoldGS	22.63	21.98	22.68	24.37	24.15	27.76	20.39	19.64	20.08
Mip-Splatting	23.65	23.49	24.97	25.27	24.49	27.69	21.38	21.23	20.66
3DGS	24.11	23.79	25.54	26.16	25.28	28.39	21.87	21.34	20.51
LightGaussian	24.21	23.94	26.95	25.62	25.91	27.45	21.82	21.38	20.60
2DGS	24.42	24.06	25.17	27.92	26.96	27.53	21.83	21.58	20.27
SplatFields3D	24.94	26.51	25.59	28.29	25.92	27.36	23.12	21.86	20.88
SplatFields3D + Ours	25.43	27.11	26.09	28.77	26.84	27.48	23.63	22.22	21.30
					SSIM '	1			
	mean	Toy	Ficus	Hotdog	Chair	Mic	Ship	Drums	Materials
SparseNeRF	-	85.65	84.30	-	89.57	92.27	75.51	82.52	83.82
SparseNeRF wo. depth	86.95	88.45	84.65	94.06	91.26	92.39	77.25	82.12	85.42
SuGaR	83.83	84.27	88.55	90.52	88.77	84.39	74.27	80.78	79.10
ScaffoldGS	85.45	83.27	90.14	89.66	88.56	95.77	70.66	83.46	82.10
Mip-Splatting	88.00	85.68	93.15	91.76	90.34	96.44	73.98	88.22	84.41
3DGS	88.27	86.30	93.65	92.19	91.23	96.49	73.89	88.48	83.93
LightGaussian	88.76	86.66	94.82	92.41	91.70	96.27	74.37	88.75	85.12
2DGS	89.51	88.42	93.61	93.79	93.26	96.37	76.52	89.38	84.72
SplatFields3D	90.32	91.34	93.70	95.09	91.14	95.95	80.25	89.85	85.26
SplatFields3D + Ours	90.73	91.75	94.25	95.26	91.49	95.98	80.90	90.27	85.94
					LPIPS	1			
	mean	Toy	Ficus	Hotdog	Chair	Mic	Ship	Drums	Materials
SplatFields3D	10.96	9.28	6.29	7.57	9.74	4.15	26.07	9.56	15.03
SplatFields3D + Ours	11.05	9.74	5.38	7.92	9.68	4.27	26.67	9.98	14.78

We also provide a detailed per-scene breakdown and additional baseline comparisons for surface reconstruction on DTU [Aanæs et al. 2016] dataset in Table 21. Our method achieves state-of-the-art performance among baselines [Dai et al. 2024b; Guédon and Lepetit 2024b; Huang et al. 2024; Kerbl et al. 2023; Yu et al. 2024d].

SA Conference Papers '25, December 15-18, 2025, Hong Kong, Hong Kong.

	Chamfer Distance per Scan ↓															
Method	24	37	40	55	63	65	69	83	97	105	106	110	114	118	122	Mean
3DGS	2.14	1.53	2.08	1.68	3.49	2.21	1.43	2.07	2.22	1.75	1.79	2.55	1.53	1.52	1.50	1.96
SuGaR	1.47	1.33	1.13	0.61	2.25	1.71	1.15	1.63	1.62	1.07	0.79	2.45	0.98	0.88	0.79	1.33
GaussianSurfels	0.66	0.93	0.54	0.41	1.06	1.14	0.85	1.29	1.53	0.79	0.82	1.58	0.45	0.66	0.53	0.88
2DGS	0.48	0.91	0.39	0.39	1.01	0.83	0.81	1.36	1.27	0.76	0.70	1.40	0.40	0.76	0.52	0.80
GOF	0.50	0.82	0.37	0.37	1.12	0.74	0.73	1.18	1.29	0.68	0.77	0.90	0.42	0.66	0.49	0.74
GOF + Ours	0.44	0.70	0.38	0.37	0.92	0.77	0.67	1.14	1.24	0.64	0.62	0.78	0.37	0.59	0.45	0.67

Table 21. Quantitative comparison on the DTU Dataset. Our method enhances GOF and achieves state-of-the-art performance.

D Limitation

Our method introduces additional computational overhead, primarily from two sources: (1) the neural network used to encode perprimitive texture fields, and (2) the extra computation required for ray-Gaussian intersection. Future work could focus on optimizing these two components to further improve efficiency.

Another limitation of our method lies in its reduced effectiveness on outdoor scenes. While it achieves strong performance on indoor datasets, the improvement is less pronounced on outdoor benchmarks such as Mip-NeRF 360. We attribute this to the limitations of the current bounded tri-plane encoding in capturing complex, large-scale outdoor variations. Future directions may explore more expressive or hierarchical neural encoding schemes to address this challenge.